5-18-2007

Fatigue Microcracking of Composite Material IM7/977-2

Michael Dana Holt
University of New Orleans

Fatigue Microcracking of Composite Material IM7/977-2

A Thesis

Submitted to the Graduate Faculty of the
University of New Orleans
in partial fulfillment of the
requirements for the degree of

Master of Science
In
Mechanical Engineering

by

Michael Dana Holt

B.S. University of New Orleans, 2004

May, 2007

Dedication

I would like to dedicate this thesis to my family. Especially my loving wife, Nicole Berthonnaud Holt, whose patience and love were critical during the preparation of this manuscript. Also to my mother, Diana Joan Holt, whose support and faith in me keep me on the right path. And finally to my father, William Penn Holt, Jr., who inspired me to accomplish all that I might. R.I.P.

Acknowledgements

I would like to acknowledge all of the people who aided and assisted me during this research program. First, my appreciation goes out to Dr. W. W. St. Cyr, the NASA Stennis Space Center Graduate Student Researcher Program's Technical Advisor, whose financial support during a portion of this research was most welcome. Second, I would like to thank my academic advisor, Dr. Melody Verges, for her guidance and direction which greatly improved the quality of this research. Also, I would like to thank the other members of my advisory committee, Drs. Paul Schilling and Paul Herrington, whose comments and support greatly assisted me during my work. Third, I would like to thank the National Center for Advanced Manufacturing for the use of the manufacturing equipment and facilities need to provide the test specimens. Last but not least, I would like to thank Lockheed Martin Space Systems Company, Michoud Operations and the Composite Products and Technology department who both employed me during the performance of this study and also provided the specimens and engineering support under the NCAM consortium. Additional thanks to Maneesh Sankar and Daryl Marse for their assistance in the lab.

Table of Contents

List of Figures

List of Tables

Acronyms and Abbreviations

UT	Ultrasonic
QI	Quasi-Isotropic
με	Micro-strain $(in/in)^{-6}$
psi	pounds per square inch
Cryo	Cryogenic
NDE	Non-Destructive Evaluation
PAN	polyacrylonitrile
NASA	National Aeronautics and Space Administration
RLV	Reusable Launch Vehicle
NCAM	National Center for Advanced Manufacturing
MIL	Military
HDBK	Handbook
CLT	Classic Laminate Theory
ANSI	American National Standards Institute
AIAA	American Institute of Aeronautics and Astronautics
COPV	Composite Overwrapped Pressure Vessel
CPS	Composite Pressurized Structure
LMSSC-MO	Lockheed Martin Space Systems Company, Michoud Operations
MPa	Mega-Pascals $(N/m^2 \times 10^6)$
N	Newtons Force
m	Meter
mm	Millimeter
$\Delta\sigma_0$	Applied Peak Load (MPa)
J	Joules (N-m)
G_m	Microcrack Energy Release Rate
G_{mc}	Critical Microcrack Energy Release Rate OR Microcrack Fracture Toughness
ΔG_m	Applied Peak Microcrack Energy Release Rate
ΔG	Applied Peak Energy Release Rate
°	Degrees
°C	Degrees Celsius
Y(D)	Energy Release Rate Scaling Factor

Abstract

The application of an ultralight linerless composite fuel tank to a man-rated, reusable launch vehicle requires greater understanding of the micro-fracture behavior which can lead to propellant permeation through the tank wall. Transverse matrix cracks in unidirectional wound, or placed, plies can provide a path for permeation of pressurized fluid if the cracks interlink from the interior to the exterior of the tank wall. Following research on an energy based fracture mechanics approach to composite microcracking, experiments in fatigue were run on IM7/977-2 cross-ply laminates. Using a modified Paris Law approach, microcracking fatigue data is presented over a wide range of applied cyclic stresses. This Paris Law plot shows an "A" value of 6.40×10^{-25} and a "B" value of 8.07 and provides a complete characterization of composite IM7/977-2 material's resistance to microcrack formation during fatigue loading.

1.0 Introduction

Composite materials have been in use for many years. Industries where composite materials are currently widely used include automotive, sports equipment, construction, boating, and aerospace. However, aerospace applications generally require higher performance, more advanced composites [1]. The main issue preventing greater use of composite materials in aerospace applications is damage tolerance. For metallic components there are many well understood analytical tools to predict life-cycle properties used in fracture control studies. However, for composite components, there are currently no widely accepted analytical tools available and structural integrity and reliability must be demonstrated through a series of expensive tests [2]. See Figure 1 for an accepted building block approach for qualification and verification of composite aerospace structures.

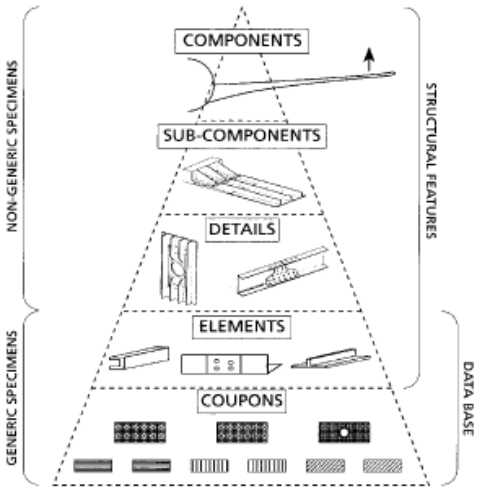

Figure 1: Building Block Testing Pyramid for aerospace composite materials showing five levels of detail each requiring its own test program [2]

The figure from MIL-HDBK-17F (Figure 1) shows a series of test programs starting with coupon testing and working upward in complexity and size until full scale flight hardware is tested to verify performance. In-between generic elements, design details and sub-components must all be tested to guide the design, validate stress models, and establish confidence in the final hardware. All of these test programs represent significant cost and schedule loads that are required to enable the benefits, such as weight savings, of composite materials for aerospace flight hardware.

Recent efforts to use continuum mechanics to understand damage propagation in composite materials have been very promising. These efforts include modeling of composite structures on multiple levels, from the micromechanics level (10^{-6} m) up to the structural level (10^{2} m). At each level structural performance is modeled based on test results [3]. This study builds upon previous fracture mechanics research into composite materials.

The material under consideration in this study is IM7/977-2 carbon fiber and epoxy resin advanced composite material. This material was laid-up with unidirectional tape in the [0/90/90/0] orientation using automated fiber placement and provided by Lockheed Martin Michoud Space Systems, Michoud Operations for the purpose of investigating microcracking behavior. The equipment and facilities used to manufacture this material were provided by the National Center for Advanced Manufacturing (NCAM).

The following sections of this chapter include a review of the literature on this topic and discuss the motivation behind the current research. Based on the conclusions and procedures from the literature reviewed, the final section of this chapter outlines the

thrust of the current work. Chapter 2 includes a discussion of the set-up and experimental procedure used in this study. Chapter 3 provides a discussion of the results of the study, including a discussion of microcrack initiation, propagation and the Paris law for composites in fatigue. Chapter 4 discusses the conclusions of this study and recommendations for further research.

1.1 Problem Background

The National Aeronautics and Space Administration (NASA) is interested in building a completely Reusable Launch Vehicle (RLV). In order to meet mission requirements, the RLV will need to be made of lightweight materials with sufficient structural integrity. Composite materials have long been used to provide weight savings over metals while still providing physical properties capable of meeting mission requirements. One application that has interested NASA and the aerospace industry is the use of composite fabricated cryogenic tanks. A large percentage of a space launch vehicle's mass is the tanks containing the cryogenic fluids. Reducing the weight of these tanks would save significant weight in the total vehicle and therefore increase the payload capability or increase the available on-board fuel thus increasing the range of the vehicle [4].

A limitation to the application of composite fabricated cryogenic tanks is the formation of defects that could lead to leakage or permeation of the cryogenic fluids. Composite materials can form small interlaminar cracks (microcracks) at tensile loads much less than those at failure. Permeation through the tank wall will likely increase as the amount of microcracking increases assuming there is an interlinking path for the fluid to pass through. The ability to qualify composite cryogenic fuel tanks depends on

the ability to quantify the extent of microcracking throughout the laminate. Therefore, it is valuable to be able to predict the extent of microcracking caused by a given load profile in flight [5].

Extensive research has been performed with quasi-isostatic loading to determine stress levels at which microcracking begins using a fracture mechanics approach [6-15]. Additional research has been performed with graphite/epoxy cross-ply laminates in fatigue [16-18]. This thesis expands upon previous work to include experimental results in fatigue for material system IM7/977-2. This polyacrylonitrile (PAN) based intermediate modulus fiber and thermoplastic toughened epoxy resin system is considered an industry favorite for unlined composite cryogenic propellant tanks [5].

IM7/977-2 is considered a good candidate for composite cryogenic propellant tanks because of previous cyro-thermal cycling testing performed for NASA's X-33 RLV program [17]. In those tests, it was determined that 10 thermal cycles of 380 °C (-255 °C to 125 °C) would not cause microcracking in quasi-isotropic laminates. However, mechanical cycling at cryogenic temperatures combined with thermal cycling tended to accelerate the formation of microcracks [19].

Matrix microcracking is the first and most innocuous damage mode observed of the various forms of damage composite materials experience, including fiber pull-out, delaminations and fiber breakage. Once a matrix crack is initiated, it extends the entire thickness of the ply being bridged by debonding of the relatively weak fiber-matrix interface. Figure 2-1 shows a schematic of two transverse matrix cracks in a cross-ply laminate. These two cracks are separated by a distance 2*a* and extend from one ply

boundary to the other through the thickness of the 90° ply group. Figure 2-2 shows the formation of a third crack between two existing cracks at a distance $2\delta t_1$ from one crack.

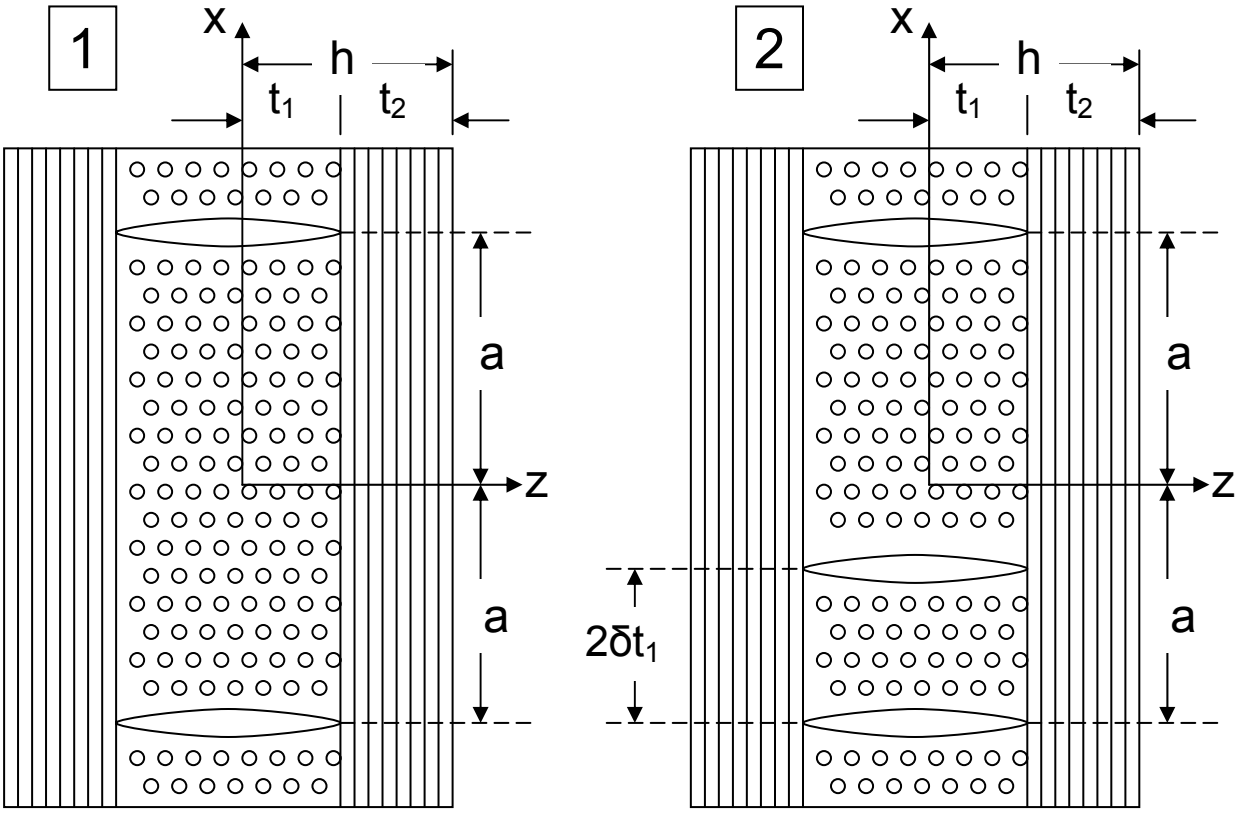

Figure 2: Matrix Cracks in a Cross-Ply Laminate separated by a distance of 2a (2-1) and the formation of a third crack at a distance of $2\delta t_1$ from one crack (2-2)

When the microcrack reaches the ply boundary, it has two options for continued flaw growth. Either a delamination crack is produced or there is fiber fracture in the adjacent 0° ply [20]. Microcracks also grow along the length of the fibers where cracking has already nucleated. These cracks tend to grow the entire length of the ply. Short microcracks are known to form in proximity to full-length off-axis microcracks, e.g. short microcracks in a 45° ply next to a full-length crack in a 90° ply in a QI laminate [21].

Microcracks can form during transverse tensile loading, fatigue, and thermal cycling. Microcracks form in plies that are off-axis to the loading direction. However, in bi-axial loading situations, such as those experienced by pressure vessels, all plies experience some transverse strain and are susceptible to microcracking [7].

Microcracks can initiate in any ply, not just 90° plies, that experiences transverse strain of sufficient magnitude. Straight microcracks tend to form rapidly and across the entire cross-section of the 90° ply. Some cracks are curved, also observed in this study, and propagate differently. Curved microcracks tend to form at the ply boundary near a previously existing straight microcrack and slowly propagate at some angle toward the earlier crack [22].

Testing of 977-2 resin with T700 fibers has experimentally determined that the strain to initiate microcracking in a transverse ply of a [0/90] laminate is 5,000 με at -196 °C and almost 9,000 με at 22 °C for 0.15 mm thick 90° plies [23, 24]. Testing of 977-2 resin with IM7 fibers has experimentally determined that the strain to initiate microcracking in a transverse ply of a [0/90] laminate is 12,000 με at 22 °C for 0.275 mm thick 90° plies [13].

With the presence of an initial microcrack or flaw, microcracks can progress with the application of elevated strain levels. Alternately, microcracks can progress with the application of fatigue even for strain levels below what is required for microcracking in static loading. In both cases, the initial microcracking density typically increases very rapidly. See Figure 3 for a schematic of microcrack progression in fatigue. The initial rapid increase of microcrack density has been associated with manufacturing defects, such as voids [9]. The initial manufacturing defects act as nucleation points for the first

few microcracks. It is difficult to model the behavior of microcracks in this region as the energy required to form a new microcrack at a pre-existing flaw is dependent on void size and geometry.

The microcrack density approaches a saturation level in static loading after the initial rapid increase in microcracks. As shown in Figure 3, in fatigue loading there is an intermediary region between rapid increase and saturation. This is a region of linear growth in microcrack density as a function of cycles. Usually the majority of microcracking in fatigue occurs during this linear region and the growth rate is associated with the material properties of the laminate in question. Like crack initiation, propagation has been observed to be dependent on ply thickness and boundary conditions with thicker plies propagating cracks more rapidly than thinner ones and plies on the outside progressing damage faster than inner plies [9, 16, 25].

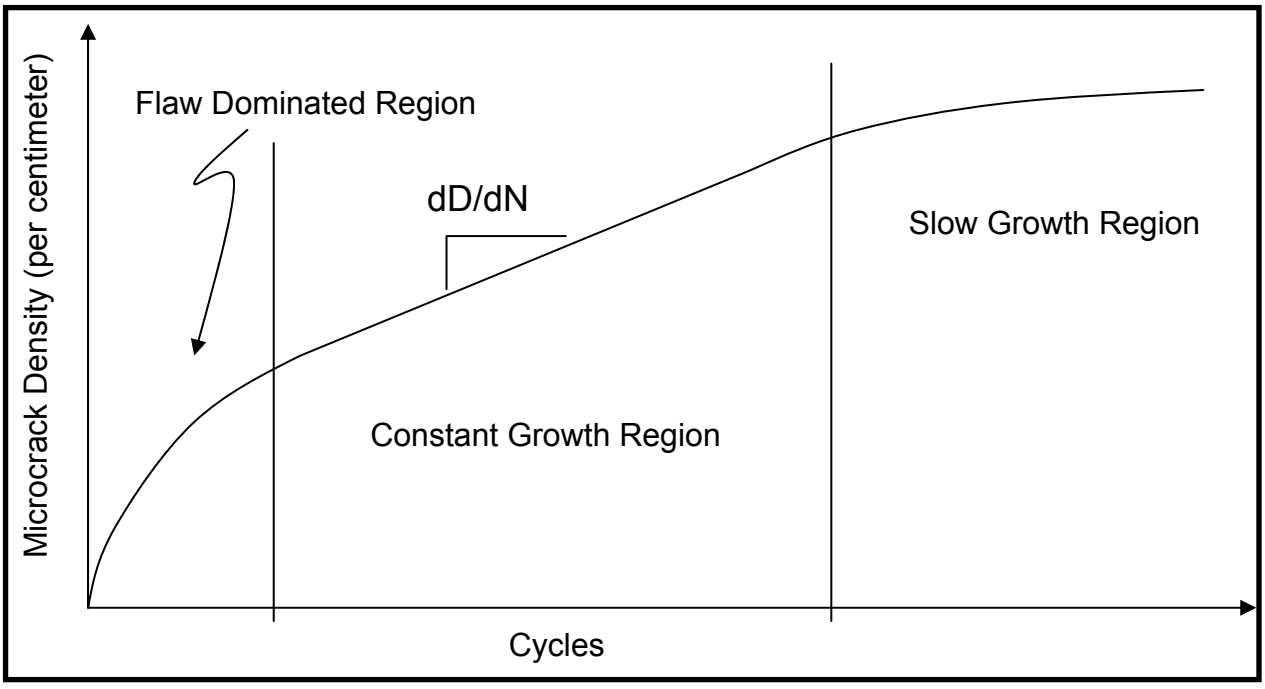

Figure 3: Schematic of Three Regions of Microcrack Propagation in Fatigue showing the flaw dominated, constant growth, and slow growth regions

1.2 Effects of Microcracks on Linerless Composite Tanks

Microcracking has the general effect on composites of reducing the stiffness and strength of the laminate, accelerating the formation of flaws over time. As the structure itself changes due to microcracking, there are likely to be interactions with other damage modes such as delamination and eventually fiber breaking [3]. Fatigue loading can result in matrix microcracks nucleating to delaminations through shear deformation at the ply interfaces [20].

The primary concern is permeation and leakage with respect to reusable linerless composite propellant tanks. The fluids contained in these tanks are hazardous, frequently toxic, flammable, or both. Therefore, any detectable leakage is likely to be unacceptable. Assuming the linerless tank has been shown to be damage tolerant, then permeation becomes the critical issue with this enabling technology. For filament wound structures, the standard is less than 10^{-4} scc/sec of gaseous He at 1% biaxial strain. It has been noted that microcracks can provide an interconnected path for fluid flow. Assuming the existence of such an interconnected pathway, then permeability tends to increase exponentially with increasing microcrack density [5].

It has also been observed that the presence of microcracks is not sufficient to guarantee permeation. In addition, the cracks must line up in such a way as to provide a torturous path for fluid flow. Knowledge of the spatial relation between microcracks is needed to predict fluid permeation through a composite laminate [21]. Indeed, permeability testing of unidirectional composite laminates under load has shown no increase in permeability prior to transverse ply failure. Or, in other words, non-cracked transverse plies act as an impermeable barrier for cryogenic propellant [26]. Therefore,

it will be useful to predict when and where microcracks are likely to form during the flight profile of any given RLV. By fully characterizing IM7/977-2 microcracking in fatigue, this study attempts to provide sufficient information to predict microcracking as a function of load profile.

1.3 Classic Laminate Theory

A baseline approach commonly used to predict microcracking initiation is the first ply failure theory. In this theory, classic laminate theory (CLT) is used to predict when the transverse strain to failure is exceeded in a 90° ply. It is assumed that when this strain level is exceeded, microcracking occurs. This theory fails for several reasons. First, testing indicates that microcracking is highly dependent on ply thickness. Thicker plies crack more easily while thinner plies do not crack prior to laminate failure. CLT predicts that strain to failure is independent of ply thickness. Moreover, classic laminate theory assumes that testing on unidirectional laminates in isolation can yield useful information regarding the transverse strain to failure. However, experimental data indicate that ply lay-up effects strain to failure [7]. Likewise, the boundary conditions of a ply affect microcrack initiation with plies on the outside of a laminate cracking at lower strain levels than predicted by CLT. Therefore, CLT and first ply failure are poor models for microcrack initiation [7, 24].

1.4 Fracture Mechanics Approach to Predicting Microcracking

A fracture mechanics approach was previously derived by Nairn because of the drawbacks associated with the first ply failure theory previously discussed [7]. Traditional fracture mechanics concerns the issue of crack growth. However, microcracks behave differently. Microcracks form nearly instantaneously and release a

finite amount of energy due to their formation. The existence of additional interacting modes of damage, including fiber pull-out, fiber breakage, and delamination make traditional fracture mechanics difficult to apply. However, a modified energy release rate theory can be applied to the formation of microcracks for the purpose of predicting the conditions in which microcracks will occur [27].

The energy release rate theory predicts that a microcrack will form when the energy that would be released by the formation of that crack reaches some critical value. This value is the critical microcracking energy release rate, denoted G_{mc}, and is called the microcracking fracture toughness. The microcracking fracture toughness, G_{mc}, is a ply lay-up independent material property that, once known, can be used to predict the conditions under which microcracking will form. Most studies use $[0_n/90_m]_s$ lay-ups for ease of testing and detection of microcracks [7].

The following section reproduces the work of Liu and Nairn [9] in determining a fracture mechanics approach for microcracking. The microcracking energy release rate can be expressed as

$$G_m = \left(\frac{E_T}{E_c} \sigma_0 - \frac{\Delta \alpha T}{C_1} \right)^2 C_3 t_1 Y(D) \tag{1}$$

where E_T is the transverse modulus of the ply, E_C is the modulus of the laminate in the direction of loading, σ_0 is the applied tensile stress, $\Delta\alpha$ is the difference between the transverse and longitudinal per ply coefficient of thermal expansion. T is the difference between the temperature and the stress free temperature, t_1 is the half thickness of the 90° ply group as shown in Figure 2, and C_1 and C_3 are constants that are functions of the material properties. $Y(D)$ is called the energy release rate scaling factor and is a

calibration factor dependent on crack density and crack spacing. Crack density is expressed as

$$D = \frac{N}{L} \tag{2}$$

where D is the crack density, N is the number of cracks and L is the length of the specimen. The energy release rate scaling factor is formally expressed as

$$Y(D) = LW \frac{d}{dA}\left[\frac{\sum_{i=1}^{N} \chi(\rho_i)}{\sum_{i=1}^{N} \rho_i}\right] = \frac{d}{dD}\left(D\langle \chi(\rho)\rangle\right) \tag{3}$$

where W is the specimen width, ρ is the non-dimensional crack spacing defined as a/t_1, a is half the distance between existing cracks as shown in Figure 2, $\chi(\rho)$ is a shape factor function, and $\langle\chi(\rho)\rangle$ is the average value of $\chi(\rho)$ over a distribution of cracks. $\chi(\rho)$ is expressed as

$$\chi(\rho) = 2\alpha\beta\left(\alpha^2 + \beta^2\right)\frac{\cosh 2\alpha\rho - \cos 2\beta\rho}{\beta \sinh 2\alpha\rho + \alpha \sin 2\beta\rho} \tag{4}$$

where α and β are constants defined by

$$\alpha = \frac{1}{2}\sqrt{2\sqrt{q} - p} \tag{5}$$

and

$$\beta = \frac{1}{2}\sqrt{2\sqrt{q} + p} \tag{6}$$

where $p = (C_2 - C_4)/C_3$ and $q = C_1/C_3$. The constants C_1, C_2, C_3, and C_4 are functions of the material properties and can be expressed as

$$C_1 = \frac{hE_C}{t_2 E_A E_T} \qquad C_2 = \frac{\nu_T}{E_T}\left(\lambda + \frac{2}{3}\right) - \frac{\lambda \nu_A}{3E_A} \tag{7}$$

$$C_3 = \frac{\lambda+1}{60E_T}\left(3\lambda^2+12\lambda+8\right) \qquad C_4 = \frac{1}{3}\left(\frac{1}{G_T}+\frac{\lambda}{G_A}\right)$$

where t_2 is the 0° ply thickness, $\lambda = t_2/t_1$, E_A is the axial per ply modulus of the material, v_A and v_T are the axial and transverse Poisson's ratios respectively, and G_A and G_T are the axial and transverse shear moduli, respectively.

To evaluate Y(D) discrete differentiation must be used. Assume that a new crack forms at some distance $\xi = 2\delta - \rho_k$ in the k^{th} crack interval. Prior to the formation of the new crack:

$$\langle\chi(\rho)\rangle = \frac{1}{N}\sum_{i=1}^{N}\chi(\rho_i) \qquad \text{and} \qquad D = \frac{N}{L}$$

and after the formation of the new crack:

$$\langle\chi(\rho)\rangle = \frac{1}{N+1}\left[\left(\sum_{i=1}^{N}\chi(\rho_i)\right)-\chi(\rho_k)+\chi(\rho_k-\delta)+\chi(\delta)\right] \qquad \text{and} \qquad D = \frac{N+1}{L}$$

Thus, the calibration function can be expressed as

$$Y(D) = \frac{\Delta\left(D\langle\chi(\rho)\rangle\right)}{\Delta D} = \chi(\rho_k-\delta)+\chi(\delta)-\chi(\rho_k) \tag{8}$$

In the laboratory it is difficult to know where the next crack will form. Therefore, some simplifying assumptions are made to aid analysis. First, it can be assumed that microcracks tend to be regularly spaced. This means that the new crack will form where the interval is near the average crack spacing, i.e., $\rho_k = 1/2t_1D$. Second, regular spacing implies that new cracks will form in the center of two already existing cracks, i.e., $\delta = \rho/2$. With these two assumptions, equation (8) simplifies to

$$Y(D) = 2\chi\left(\frac{\rho}{2}\right)-\chi(\rho) = 2\chi\left(\frac{1}{4t_1D}\right)-\chi\left(\frac{1}{2t_1D}\right) \tag{9}$$

Utilizing equation (9) for Y(D) and equation (1) for G_m it is possible to analyze data for the formation of microcracks. The more formal equation (8) is used in static loading to determine critical microcrack fracture toughness so as to obtain greater accuracy. Equation (9) is used in fatigue specimens because the simplifying assumptions do not usually adversely affect the results for dynamic testing [16].

1.4.1 Quasi-isostatic loading

The specimen is brought to a predetermined stress level and the number of microcracks is counted to determine the density during static loading. The specimen is then loaded at ever higher evenly spaced stress levels and the procedure is repeated. By experimentally obtaining microcrack density as a function of applied loading and utilizing equations (8) and (1) the microcracking fracture toughness for a specific composite system can be determined. This procedure for the analysis of microcracking data has been used by multiple researchers to obtain the microcracking fracture toughness for over 16 composite material systems [7, 13]. Verges, et. al., implemented this procedure to investigate IM7/977-2 $[0/90]_s$ laminates in static loading [6]. Table 1 compiles critical microcracking fracture toughness data for these 16 composite material systems.

Table 1: Microcracking Fracture Toughness of Several Composite Materials

Composite Material (Fiber/Resin)	G_{mc} (J/m^2)	References
E-Glass/Epoxy	200	[8]
AS4/3501-6	220	[9, 10]
IM7/954-2A	240	[11]
AS4/Polycyanate	430	[12]
AS4/Polysulfone	450	[11]
IM7/8551-7	525	[12]
AS4/Tactix® 556	550	[12]
IM7/977-2	600	[13]
Scotch Ply 1003 (E-Glass/Epoxy)	650	[7]
T300/934	690	[9]
G40-800/rubber modified Polycyanate	720	[12]
AS4/Tactix® 696	825	[12]
IM6/Avimid® K	960	[9, 11, 14, 15]
IM7/PETI5	1080	[15]
T300/977-2	1800	[9]
AS4/PEEK	3000	[9]

See Figure 4 for a plot of microcrack density versus applied load for IM7/977-2 $[0/90]_s$ laminates. For these laminates, cracks initiated at around 1000 MPa of applied load and then microcrack density increased very rapidly with further applied load. The crack density saturated at around 1.3 mm^{-1} [6]. The critical microcrack fracture toughness for IM7/977-2 was determined to be 600 J/m^2 [13].

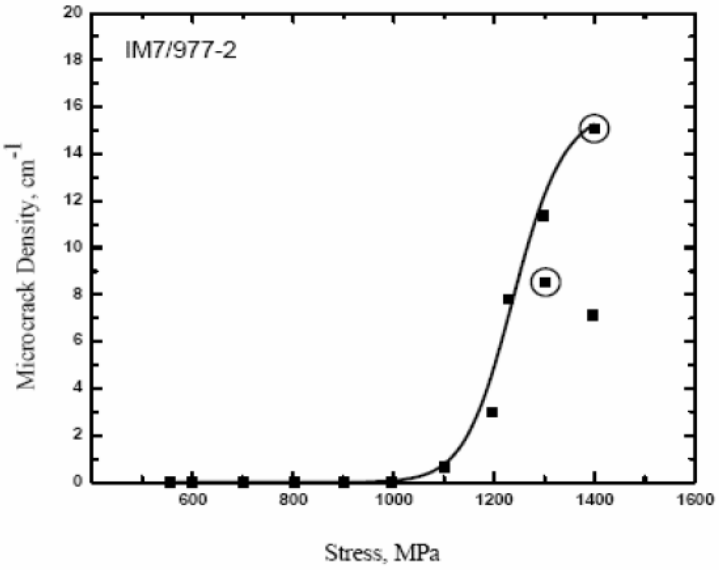

Figure 4: Microcrack Density Versus Applied Stress for IM7/977-2 [6]

1.4.2 Fatigue loading and the Paris law

The conventional Paris Law approach relates the crack tip growth of an existing flaw to the applied stress intensity factor, ΔK, using a power law $da/dN = n(\Delta K_I)^m$, where da/dN is the crack tip growth rate as a function of cycle number, ΔK_I is the applied cyclic mode 1 stress intensity factor, and n and m are fitting parameters [28, 29]. A plot of the Paris law has a threshold region, a linear region, and a critical failure region, called regions I, II, and III respectively. See Figure 5 for a generic schematic of conventional Paris law crack tip growth showing the three regions. The first region is where the threshold stress intensity factor, K_{th}, resides. Below K_{th}, no flaw growth is caused due to fatigue loading whereas increased application of K_I causes a rapid increase in crack tip growth per cycle that gradually decreases into the linear region. Region II is called the linear region because the curve appears linear on a log – log plot and the slope of the line is the power factor in the Paris law, sometimes called an “m” value. As the applied stress intensity factor is increased near the critical value, K_{Ic}, the slope begins to rapidly increase as the material nears failure in Region III.

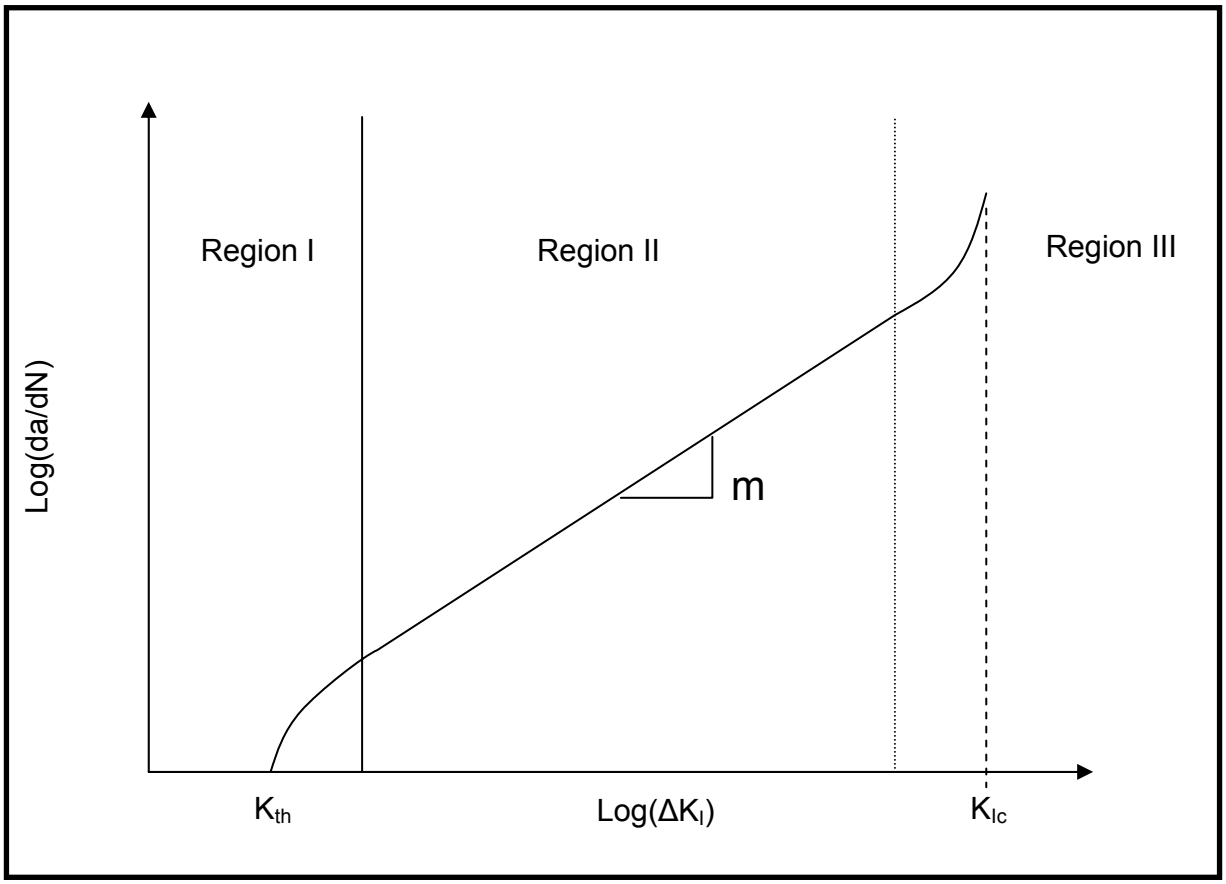

Figure 5: Schematic of the Conventional Paris Law showing applied stress intensity factor versus crack tip growth rate as a function of number of cycles on a log – log plot indicating the three regions of flaw growth

An applied *ΔG* is substituted for *ΔK* when composites in fatigue are analyzed because of the difficulties associated with using standard fracture mechanics in composite materials previously discussed. Previous work by Liu and Nairn [16] has shown that microcracks can form at stress levels much lower than those required to meet the critical microcrack energy release rate for materials loaded in fatigue. They have used a modified Paris Law approach where the rate of change in microcrack density as a function of cycles is given by

$$\frac{dD}{dN} = A\left(\Delta G_m\right)^B \tag{10}$$

where *A* and *B* are power law fitting parameters and are properties of the material [16]. On a log – log plot of equation (10), the parameter *A* will be the intersection of the ordinate and the parameter *B* will be the slope of the curve. Previous research by Liu [16] has determined that the factor *B* for graphite/polyimide IM6/Avimid is 5.47 and for graphite/epoxy T300/934 is 2.34. This factor *B*, similar to the *m* value shown in Figure 5, is of interest because it is the slope of the curve in region II of the Paris law.

As described previously in section 1.1 and Figure 3, for composite materials in fatigue there have been observed three distinct regions of microcrack density growth. The first is a flaw dominated region where the microcrack density increases rapidly as a function of number of cycles due to the presence of initial manufacturing imperfections. Next, there is a constant growth region where the slope of the microcrack density versus number of cycles curve is linear. The *dD/dN* in equation (10) refers to this linear slope in the constant growth region and is the region of interest. Finally, at higher microcrack densities there is a slow growth region associated with microcrack saturation where the number of cycles required to cause another microcrack increases very rapidly [16].

1.5 Objective of this Study

The primary purpose of this research is to accurately determine the power law fitting parameters, A and B, for composite material system IM7/977-2 to provide a complete predictive model of this material system's resistance to microcrack formation during fatigue loading. Using these fitting parameters and equation (10) it should be possible to perform a life cycle analysis and predict the microcrack densities of IM7/977-2 propellant tanks and to predict the leakage rate through their damage networks [30,

31]. As noted by Liu [16], microcrack density as a function of number of cycles in the linear region is required for determining the microcrack density growth rate as a function of applied energy release rate.

A second objective of this study was to obtain microcracking data for IM7/977-2 graphite/epoxy cross-ply laminates in fatigue at various stress levels. This would expand upon previous research by Verges [6] of quasi-isostatic loading of IM7/977-2 and by Nairn [16] of fatigue loading of other graphite/epoxy cross-ply laminates.

2.0 Experimental Procedure

2.1 Specimen Fabrication

2.1.1 Parent panel

The specimens in this study were fabricated from a 12 inch by 12 inch panel provided by Lockheed Martin Michoud Space Systems, Michoud Operations. The panel was fabricated at the National Center for Advanced Manufacturing (NCAM) using unidirectional tape under vacuum bag with an autoclave cure. Standard C-scan ultrasonic NDE was performed post-cure and no indications of initial manufacturing defects were identified. The panel is a four ply [0, 90, 90, 0] lay-up with a total thickness of 0.55 mm. The calculated Cured Ply Thickness (CPT) is therefore 0.1375 mm.

2.1.2 Sub-panels

The panel was quartered and each quadrant numbered in Roman numerals clockwise from the top right. Each quadrant was further quartered and numbered in like fashion as before. Specimens were then machined from each sub-quadrant into 60 mm x 5 mm sections.

2.1.3 Identification

The specimen identification system is a series of four numbers, the first and last being Arabic and the middle two being Roman. The first Arabic number designates the panel and material from which the specimen was machined. The second two Roman numerals refer to the quadrant and sub-quadrant respectively that the specimen was machined from. The last Arabic number refers to the specific specimen and the order it was machined from the sub-panel. All specimens in this study were cut from the top-left

sub-quadrant of the top-right quadrant of the IM7/977-2 panel provided in the batch from LMMSS and are numbered 2-I-IV-1 through 2-I-IV-12.

2.1.4 Machining

During preparation sub-panel 2-I-I was separated from 2-I-IV with dry cutting using the MK tile saw. Specimens were then machined from 2-I-IV using a circular diamond saw with continuous lubricant to ensure proper dimensions and heat removal. The blade of the cutter is a diamond metal bonded, wafer blade. Each specimen's width and thickness were measured across the length of each. Refer to table 2 for the final dimensions of each specimen tested.

2.1.5 Polishing

One edge of each specimen was polished to provide sufficient surface condition quality for optical microscopy. The specimens were polished with P-2400 grit silicon carbide polishing paper with a back-and-forth motion while applying pressure over a flat surface. A best effort was made to keep the specimen normal to the paper surface while polishing. It was frequently necessary to re-polish after specimen tabbing. In this case, the polishing paper was wrapped around a metal block and placed on the edge surface to be re-polished. Once again, a back-and-forth motion while applying pressure was made to improve the surface quality before testing.

2.1.6 Tabbing

Aluminum tabs were bonded to both ends of each specimen to assist in transferring load from the friction-grip wedges to the specimen without crushing or slipping. The tabs were sheared from 20 gauge (0.80 mm) sheet into approximately 10 mm x 20 mm rectangles. Bonding surfaces, both tab and composite, were lightly

sanded and cleaned prior to bonding. The tabs were bonded using Loctite E-120HP Hysol two part epoxy adhesive mixed using a static nip-point mixer. Glass beads measuring 0.008 inches (0.2 mm) in average diameter were lightly sprinkled onto the adhesive prior to clamping in order to control bond-line thickness and avoid squeeze out of the adhesive. The tabs were clamped together using two small binder clips per tab-end. A twenty-four hour, room temperature cure was used to set the adhesive. Excess adhesive was removed from tab edges using a razor blade, while excess adhesive was remove from tab surfaces using 120 grit sandpaper. See Figure 6 for examples of completed specimens after fabrication.

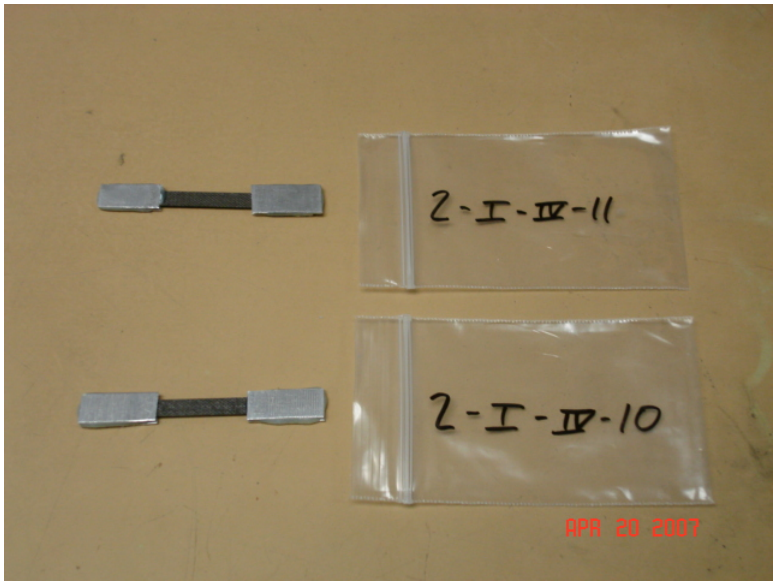

Figure 6: Fatigue Microcracking Specimens After Fabrication

2.2 Experimental Setup

Fatigue loading was performed using a small tensile sub-stage with a 2000 lbs. capability. The test setup is comprised of the Newport tensile sub-stage, ADMET data acquisition system, ProScope digital microscope, MTestWindows mechanical testing software also from ADMET, inc. and Luxus digital imaging software from Lenox

Softworks, inc. See Figure 7 for a picture of the experimental setup and Figure 8 for a close up of the tensile sub-stage.

Figure 7: Experimental Setup

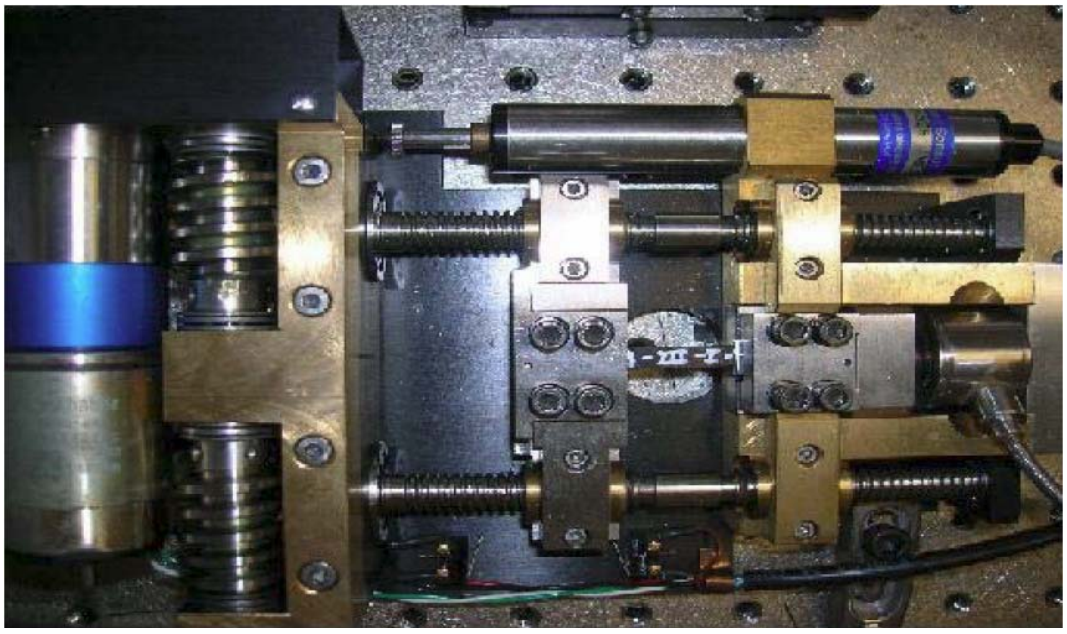

Figure 8: Close-Up of the Tensile Sub-Stage

2.2.1 MTestWindows software

The standard MTestWindows screen has four small, and one larger, windows. The four small windows display the load on the specimen, stress, displacement, and strain. Each of the four windows has displays for the current "live" value, peak value, and rate of change. The large fifth window is a load versus time graph. See Figure 9 for a picture of the live test window.

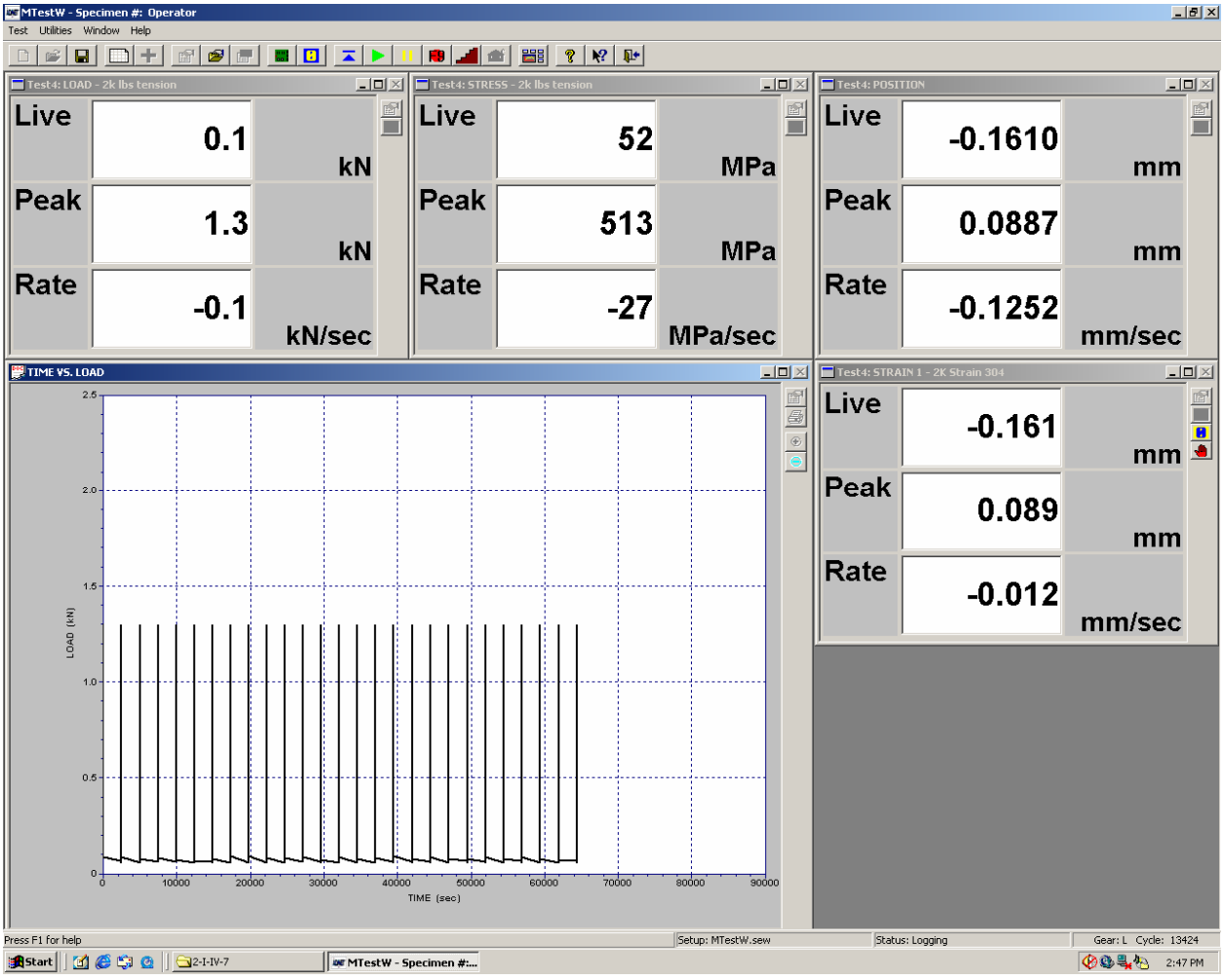

Figure 9: MTestWindows Live Test Screen and Sub-Windows

The test setup window can be accessed from the test window toolbar and gives options for display, units, data acquisition, analysis, specimen information, graphing,

servo parameters, and servo profile. See Figure 10 for an example of the test setup window.

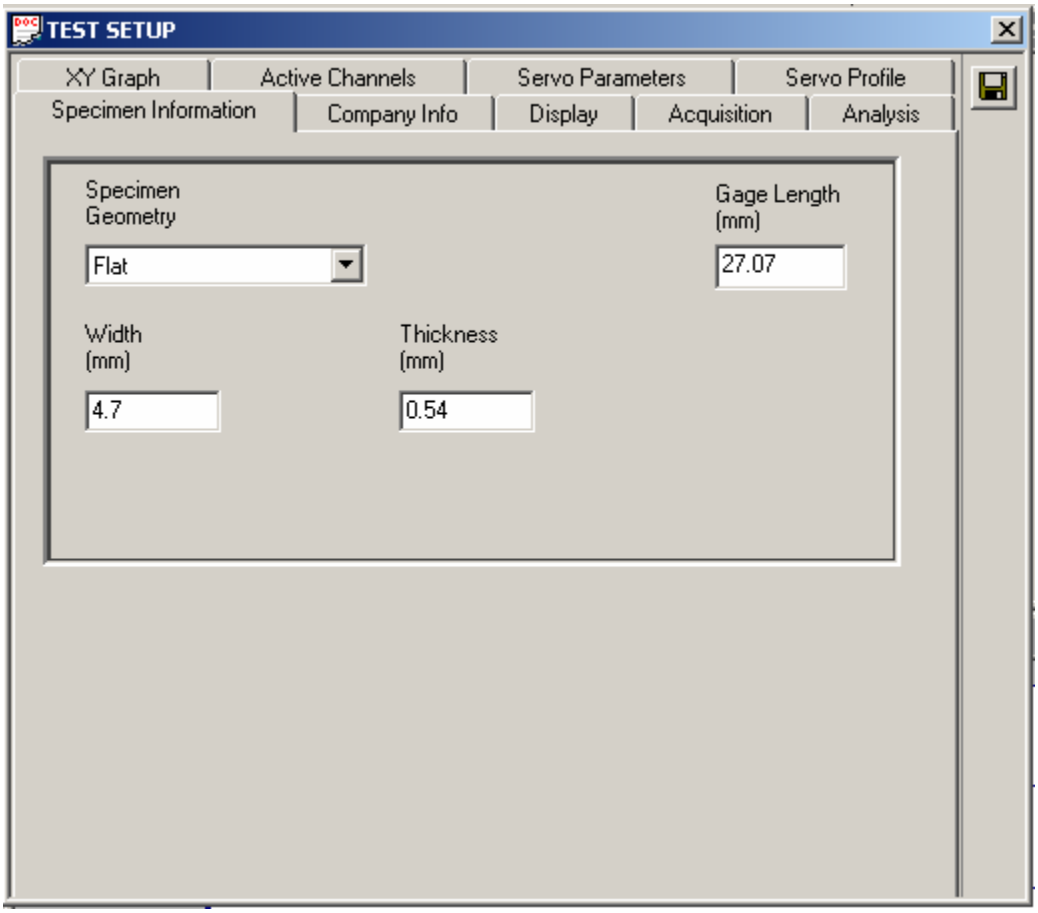

Figure 10: Test Setup Window Open to the Specimen Information Tab

Inside the test setup window, the data acquisition tab gives options for defining sample break, initiate acquisition threshold, logging rate and data saving directory. Sample break was defined as 0% of peak load so as not to interrupt the test during cycling. Data acquisition threshold was defined as 0.4 kN so as not to pass threshold during bolt tightening. The data logging rate was set to 10 samples per second. The data was set to save to a folder labeled for each specimen tested in turn. See Figure 11 for an example of the data acquisition tab.

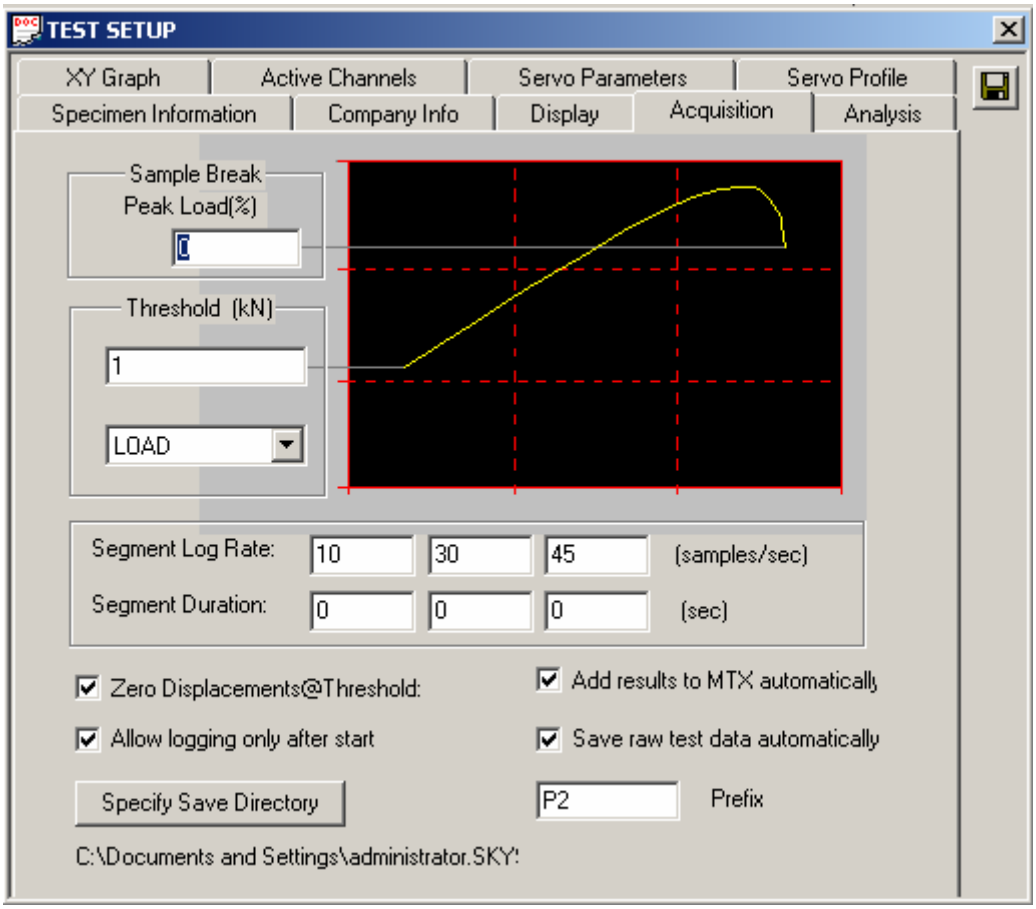

Figure 11: Test Setup Window Open to the Data Acquisition Tab

The servo parameters tab gives options for defining preload level, preload rate, jog speed, home rate, post test action, and access to the PID parameters. Preload level was defined as approximately 0.2 kN below peak cycle load level for any given specimen test. See Figure 12 for an example of the servo parameters screen.

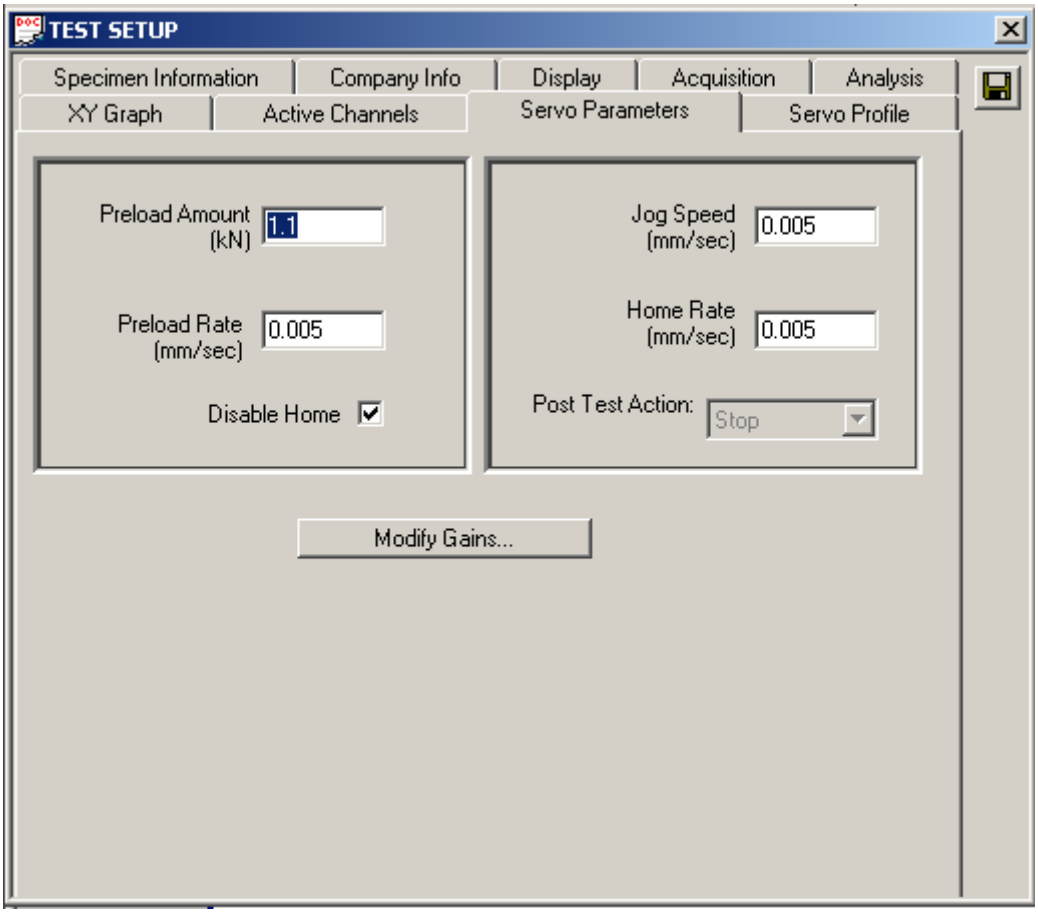

Figure 12: Test Setup Window Open to the Servo Parameters Tab

The servo profile tab gives options for servo mode (monotonic, segmented, cyclic), each of which has further options to control test parameters. These tests use the cyclic mode exclusively. The cyclic screen has options for number of cycles, logging option, ramp rate and control, peak level, and control. These tests used load control for ramp as well as peak control. Minimum valley was 0.1 kN to prevent overshoot from putting the specimen in compression. Peak values varied from specimen to specimen. The number of cycles logged is limited by the available memory. To prevent the test from being prematurely aborted due to file size, the number of cycles between data logging is limited to keep the number of cycles logged to 100. See Figure 13 for an example of the servo profile screen.

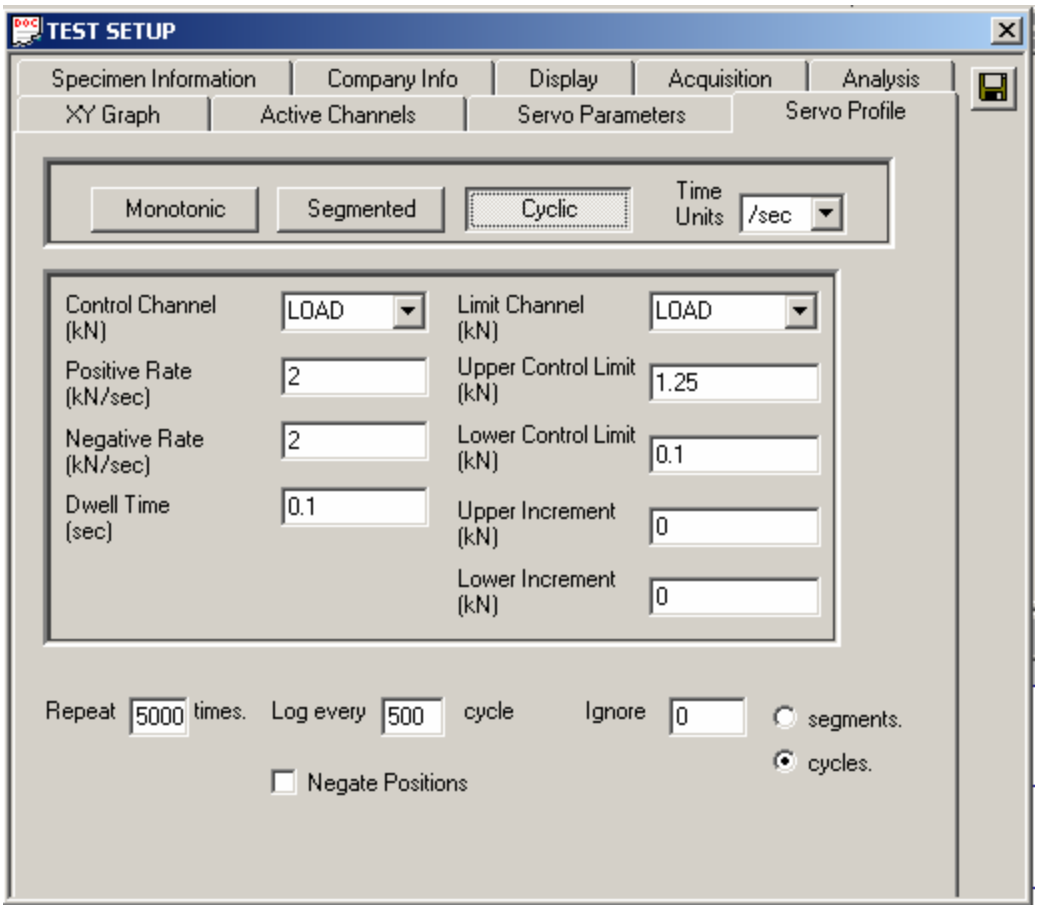

Figure 13: Setup Window Open to the Servo Profile Tab

2.2.2 Optical microscopy

The ProScope digital USB microscope has a 200x magnification lens and was used for all the optical microscopy during this study. The still capture images have a 640 x 480 pixel resolution. The microscope was mounted on a movable stand parallel to the test sub-stage and focused on the edge of the mounted specimen. The movable stand was spring loaded and outfitted with a micrometer which was used to measure the span of parallel movement during the optical scan for microcracks. A limited length of the specimen edge was visible with the microscope due to space constraints caused by the rather short focal length of the microscope and the crosshead span,. This length

is called the optical length as opposed to the gauge length measured previously. See Figure 14 for a picture of the optical microscope setup.

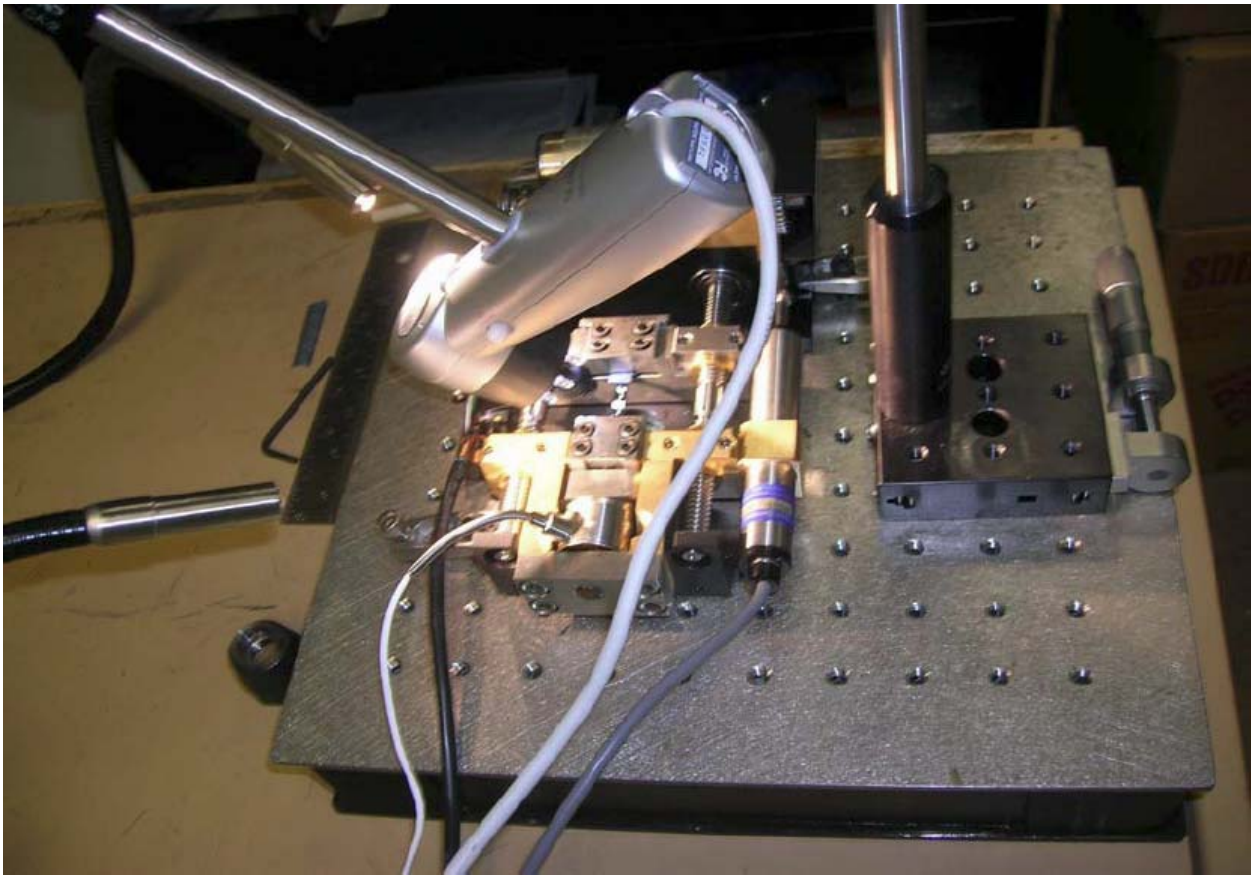

Figure 14: Optical Microscope Setup

A high intensity fiber-optic illuminator was used to assist visibility of microcracks. A “shadow” method of illumination was used where the light is directed at the edge of the specimen obliquely. This causes the surface of 90° plies to appear darks and the cracks therein to appear as bright lines. See Figure 15 for an example of this “shadow” technique.

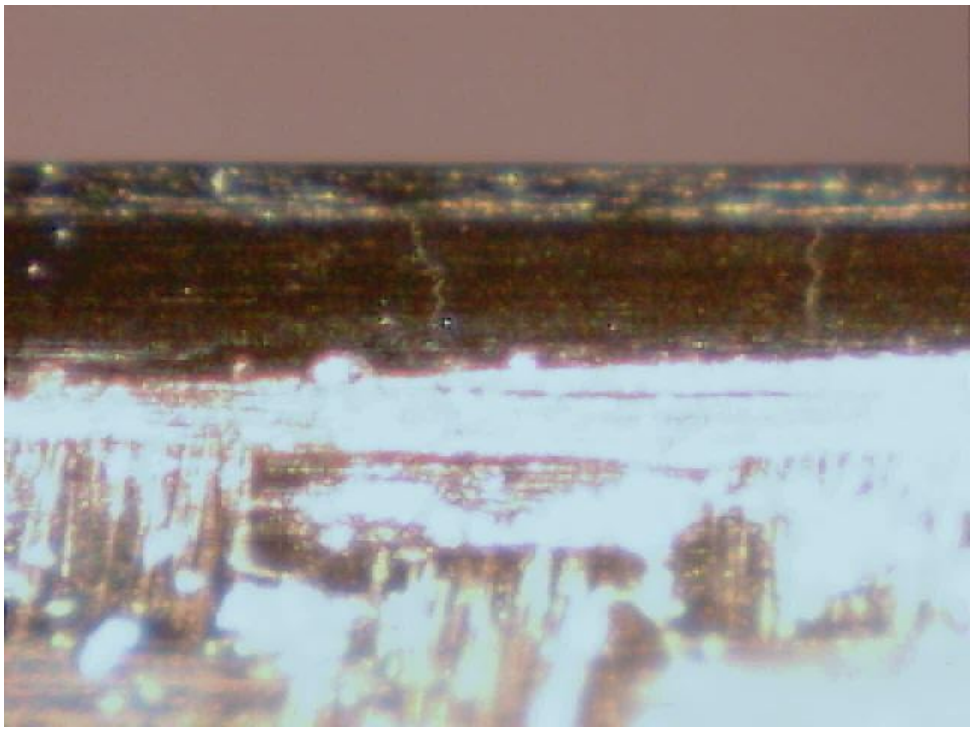

Figure 15: Oblique Illumination

2.3 Procedure

2.3.1 Setup

The PC is booted up and logged onto. The data acquisition system is turned on and placed in the tension mode. Once booted, the MTestWindows software and Luxus imaging software are run. The specimen is placed in the clamps and the left bolts are hard tightened. The test setup window is opened and the specimen information is input in the specimen information tab. Then the servo profile tab is opened and the number of cycles, peak load, and “log every _ cycle” field is filled out to limit the number of cycles logged to 100. Then the servo parameters tab is opened and the preload is set to 0.2 kN below peak cyclic load and post test action is set to stop. This test is saved and the test setup window closed. The new test button is pressed, which tares all values in the test window. When test status is ready, the right-hand bolts are hand

tightened so that they may be loosened easily to relieve stress. Then the pre-load is applied to assist the visibility of microcrack detection.

2.3.2 Optical scanning

The microscope is focused on the edge of the specimen and then the stage is moved until the microscope touches the left crosshead. The leftmost image is captured. The image can be focused by applying a small amount of manual pressure to the cantilevered beam to which the camera is mounted. The field of view for each picture is 1.375 mm of specimen edge length. After each image capture, the camera is translated parallel to the specimen edge 0.125 mm by use of the micrometer outfitted to the spring loaded stage. After translation, another image is captured and the process is repeated until the right crosshead interferes with further camera movement. Depending on specimen length it was possible to capture 13, 14, or 15 images per scan. These numbers of images correspond to 15.000 mm, 16.250 mm, and 17.500 mm of stage travel respectively. This yields optical lengths of 16.375 mm, 17.625 mm, and 18.875 mm respectively.

2.3.3 Specimen fatigue

It is simply a matter of clicking the test start button on the test screen to begin cycling, since the specimen has already been put in tension during setup. Cycle time is dependent upon peak load, but typically ranged from 5 to 10 seconds per cycle. Total cycling time is highly dependent upon the number of cycles between optical scans. It was frequently necessary to be at the tensile sub-stage when cycling completed to prevent test specimen from going into compression as the test ended.

The fatigue tests were performed under constant load conditions. Peak load varied from fatigue segment to fatigue segment, but stayed within ±2 MPa of the reported nominal value. The minimum load was low enough to be nearly zero without risking overshooting and putting the specimen into compression. Therefore, $\Delta\sigma = \sigma_{max}$ is an accurate assumption for the purposes of this thesis. The material testing system used is best suited for low cycle fatigue with the per cycle time being relatively high. Higher peak loads took longer per cycle than lower peak load cycles. High cycle, low stress fatigue tests took much longer than the low cycle, high stress tests and extended for weeks of constant testing. See table 2 for specimen geometry, peak stresses, and cyclic frequency. Two specimens were cycled to failure and the remaining specimens were cycled to a pre-determined microcrack density.

Table 2: Specimen and Test Data

Specimen ID	Width (mm)	Thickness (mm)	Area (mm^2)	Gauge Length (mm)	Optical Length (mm)	Peak Stress (MPa)	Frequency (Hz)
2-I-IV-3	4.81	0.51	2.4531	19.82	16.375	875	0.111
2-I-IV-4	4.77	0.51	2.4327	21.40	17.625	845	0.093
2-I-IV-5	4.32	0.53	2.2896	24.90	17.625	810	0.136
2-I-IV-6	4.66	0.53	2.4698	20.73	16.375	630	0.177
2-I-IV-7	4.70	0.54	2.5380	27.07	17.625	511	0.186
2-I-IV-8	4.94	0.54	2.6676	23.18	16.375	850	0.122
2-I-IV-9	4.48	0.53	2.3744	24.62	16.375	955	0.111
2-I-IV-10	4.67	0.54	2.5218	23.11	16.375	1030	0.101
2-I-IV-11	4.77	0.54	2.5758	25.21	18.125	1095	0.091
2-I-IV-12	4.64	0.53	2.4592	26.07	18.875	740	0.142

3.0 Discussion of Results

3.1 Microcrack Energy Release Rate

It is possible to calculate the microcracking energy release rate given the peak load and microcrack density. For cyclic loading where $\Delta\sigma = \sigma_{max}$, ΔG_m is equal to G_m at peak load. To calculate ΔG_m, it was necessary to use a series of material properties collected from various sources. The properties listed in table 3 were collated by B. Hottengada and were used in the analysis of the microcracking energy release rate [13].

Table 3: Material Properties for IM7/977-2 [13]

Property	Symbol	Value
Axial Lamina Modulus	E_a	159 GPa
Transverse Lamina Modulus	E_t	9.2 GPa
Axial Laminate Modulus	E_c	84.2 GPa
Axial Shear Modulus	G_a	4.37 GPa
Transverse Shear Modulus	G_t	2.57 GPa
Axial Lamina Coefficient of Thermal Expansion	α_a	-0.09×10^{-6}/°C
Transverse Lamina Coefficient of Thermal Expansion	α_t	28.8×10^{-6}/°C
Axial Lamina Poisson's Ratio	ν_a	0.253
Transverse Lamina Poisson's Ratio	ν_t	0.456
Difference from Stress Free Temperature	T_{eff}	-125 °C
Lamina Thickness	t_1	0.1375 mm

Lockheed Martin Space Systems Company, Michoud Operations provided the moduli and Poisson's ratio properties. The CTE properties used are common for graphite/epoxy laminates typically studied [9]. The stress free temperature is the difference between room temperature and the cure temperature. The per-ply lamina thickness was provided by the material supplier, Cytec Engineered Materials [32]. Using these properties and independently tested crack density versus load data, Hottengada [13] calculated the microcrack fracture toughness of IM7/977-2 to be

approximately 600 J/m^2. These calculations were double checked by performing a separate analysis using Microsoft Excel. For example, a [0 / 90 / 90/ 0] IM7/977-2 specimen, measuring 4.84 mm by 0.55 mm by11.375, was loaded to 1095 MPa. At this load, 5 cracks per centimeter were observed. The solution for the energy release rate follows:

Given: D = 0.5 mm^{-1}; σ_0 = 1095 MPa; Table 3 properties

Find: G_m

Solution: $\lambda = t_2/t_1 = 1$, since ply thickness is constant.

Likewise, $h = t_2 + t_1 = 2t = 2 * 0.1375$ mm = 0.275 mm.

So,

$$C_1 = \frac{hE_C}{t_2 E_A E_T} = \frac{0.275 \times 84.2}{0.1375 \times 159 \times 9.2} = 0.1151\left(GPa^{-1}\right)$$

$$C_2 = \frac{\nu_T}{E_T}\left(\lambda + \frac{2}{3}\right) - \frac{\lambda \nu_A}{3E_A} = \frac{0.456}{84.2}\left(1 + \frac{2}{3}\right) - \frac{1 \times 0.253}{3 \times 159} = 0.0821\left(GPa^{-1}\right)$$

$$C_3 = \frac{\lambda + 1}{60E_T}\left(3\lambda^2 + 12\lambda + 8\right) = \frac{1+1}{60 \times 9.2}\left(3 \times 1^2 + 12 \times 1 + 8\right) = 0.0833\left(GPa^{-1}\right)$$

$$C_4 = \frac{1}{3}\left(\frac{1}{G_T} + \frac{\lambda}{G_A}\right) = \frac{1}{3}\left(\frac{1}{2.57} + \frac{1}{4.37}\right) = 0.2060\left(GPa^{-1}\right)$$

$p = \dfrac{C_2 - C_4}{C_3} = \dfrac{0.0821 - 0.2060}{0.0833} = -1.4868$, and $q = \dfrac{C_1}{C_3} = \dfrac{0.1151}{0.0833} = 1.3815$

$\dfrac{4q}{p^2} = \dfrac{4 \times 1.3815}{-1.4868^2} = 2.4997 > 1$ so,

$$\alpha = \frac{1}{2}\sqrt{2\sqrt{q} - p} = \frac{1}{2}\sqrt{2\sqrt{1.3815} + 1.4868} = 0.9795$$

$$\beta = \frac{1}{2}\sqrt{2\sqrt{q} + p} = \frac{1}{2}\sqrt{2\sqrt{1.3815} - 1.4868} = 0.4647$$

$$\rho = \frac{1}{2t_1 D} = \frac{1}{2 \times 0.1375 \times 0.5} = 7.2727 \text{ and } \frac{\rho}{2} = \frac{7.2727}{2} = 3.6364$$

$$\chi(\rho) = 2\alpha\beta\left(\alpha^2 + \beta^2\right)\frac{\cosh 2\alpha\rho - \cos 2\beta\rho}{\beta \sinh 2\alpha\rho + \alpha \sin 2\beta\rho}$$

$$= 2 \times 0.9795 \times 0.4647\left(0.9795^2 + 0.4647^2\right)\frac{\cosh(2 \times 0.9795 \times 7.2727) - \cos(2 \times 0.4647 \times 7.2727)}{0.4647 \times \sinh(2 \times 0.9795 \times 7.2727) + 0.9795 \times \sin(2 \times 0.4647 \times 7.2727)} = 2.3025$$

$$\chi\left(\frac{\rho}{2}\right) = 2 \times 0.9795 \times 0.4647\left(0.9795^2 + 0.4647^2\right)\frac{\cosh(2 \times 0.9795 \times 3.6364) - \cos(2 \times 0.4647 \times 3.6364)}{0.4647 \times \sinh(2 \times 0.9795 \times 3.6364) + 0.9795 \times \sin(2 \times 0.4647 \times 3.6364)} = 2.3079$$

$$Y(D) = 2\chi\left(\frac{\rho}{2}\right) - \chi(\rho) = 2 \times 2.3079 - 2.3025 = 2.3134$$

$$G_m = \left(\frac{E_T}{E_c}\sigma_0 - \frac{\Delta\alpha T}{C_1}\right)^2 C_3 t_1 Y(D)$$

$$= \left(\frac{9.2}{84.2} \times \frac{1095}{1000} - \frac{\left(2.88 \times 10^{-5} + 9.00 \times 10^{-8}\right) \times (-125)}{0.1151}\right)^2 \times 0.0833 \times 0.1375 \times 2.3134 \times 10^6 = 604.5\left(\frac{J}{m^2}\right)$$

Further inspection of equation (1) will show that, for a given load, temperature, lay-up, material system, etc., the applied microcracking energy release rate is a function of microcrack density in the form of the shape factor function, *Y(D)*. Figure 16 is a graph showing *Y(D)* as a function of crack density that was derived using the material properties in table 3 and equation (9). Observe that the shape factor is constant up to about 4 cracks per centimeter, then increases slightly, and then begins a steep decline at or before 8 cracks per centimeter.

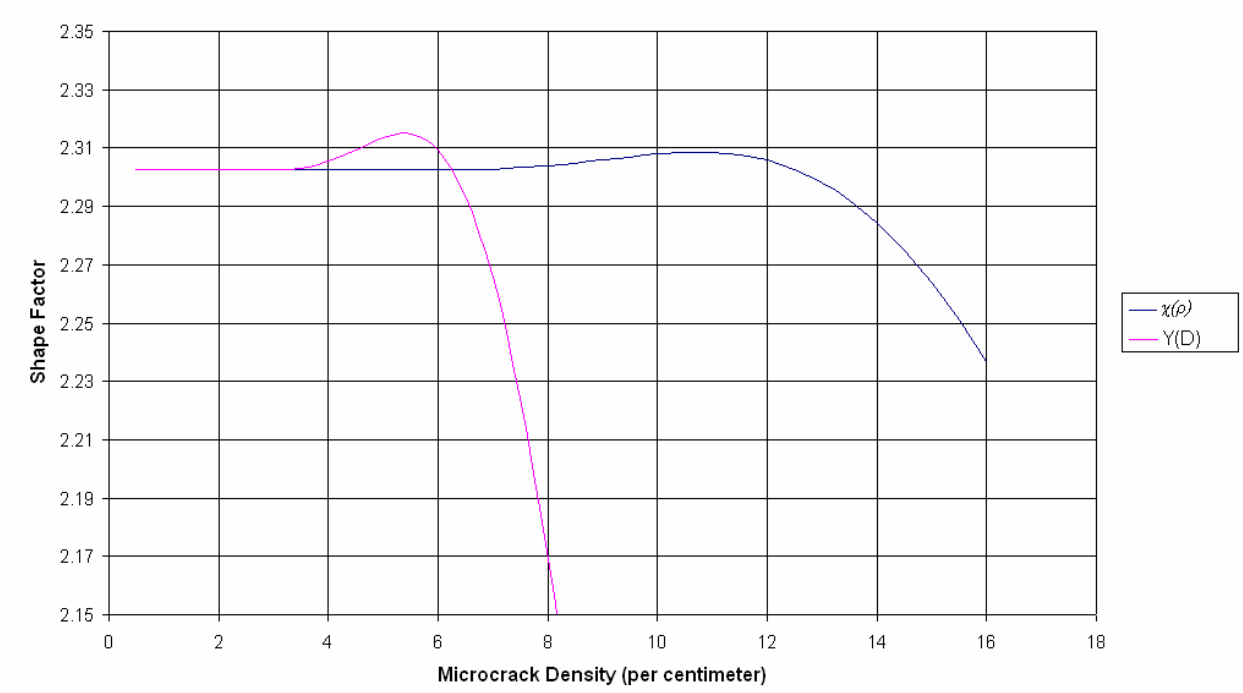

Figure 16: Shape Factors, Y(D) & χ(ρ), as Functions of Microcrack Density

3.2 Strain to Initiate Microcracking

The microcrack initiation data that can be used to determine typical strain to initiate microcracking as a percentage of strain to failure for static loading are also of interest. Table 4 contains stress to initiate microcracking and stress to failure for a series of IM7/977-2 [0 / 90]$_s$ laminates [13]. From this data it can be seen that, assuming a constant modulus, the strain to initiate microcracking is on average 85% of ultimate capability for cross-ply laminates of this ply thickness. This roughly corresponds to the strain to initiate microcracking for T700/977-2 cross-ply laminates [22]. More importantly, this strain is well above any allowable as 1.5 is the typical industry standard factor of safety for composite pressurized structures [33, 34]. It should be noted at this point that cross-ply laminates are stronger than the more realistic QI laminates because 50% of the plies are in the axis of loading. As observed

previously, microcracking can initiate at much lower strain levels when laminates are transversely loaded in fatigue. This indicates that any future RLV composite fuel tank will likely need to be analyzed in fatigue for microcrack density growth rates and their relation to permeability.

Table 4: Stress to Initiate Microcracking in IM7/977-2 Cross-Ply Laminates [13]

Specimen	Crack Initiation Stress (MPa)	Ultimate Stress (MPa)	Strain to Initiate Microcracking (% of ult.)
2-I-II-5	1029	1133	91
2-I-II-6	1015	1222	83
2-I-II-7	1005	1266	79
2-I-II-1	1054	1322	80
2-I-II-3	1026	1208	85
2-I-II-9	1065	1180	90
		Average:	85

3.3 Microcrack Propagation

A single specimen (2-I-IV-3) was selected to be cycled at 875 MPa until failure in order to acquire a comprehensive plot of microcrack density by cycle number. This test was stopped periodically and the specimen edge was inspected. As expected, microcrack density increased with number of cycles. The specimen failed at 23,825 cycles. Figure 17 shows the plot of microcrack density versus number of cycles for this specimen. Note that applied microcrack energy release rate (the red line in Figure 17) is also a function of crack density as well as applied load. Also observe that ΔG, calculated from equation (1), is constant for a wide range of microcrack densities. After reaching between 0.75 to 0.80 mm^{-1}, ΔG exhibits a steady decline to some low value as the shape factor, as $Y(D)$ begins its rapid decline. Corresponding to this decline, there is a rapid increase in the number of cycles required to induce microcracking that

represents microcrack saturation in the specimen. The microcrack energy release rate as a function of crack density graph will be the same for all specimens, except shifted up or down based on applied $\Delta\sigma$. Observe that as ΔG decreases due to increased microcrack density beyond 8 cracks per centimeter, the slope of the microcrack density versus number of cycles increases dramatically. This is predicted by the Paris Law described by equation (10), e.g. that a decrease in applied ΔG will cause an exponential decrease in the microcrack density growth rate.

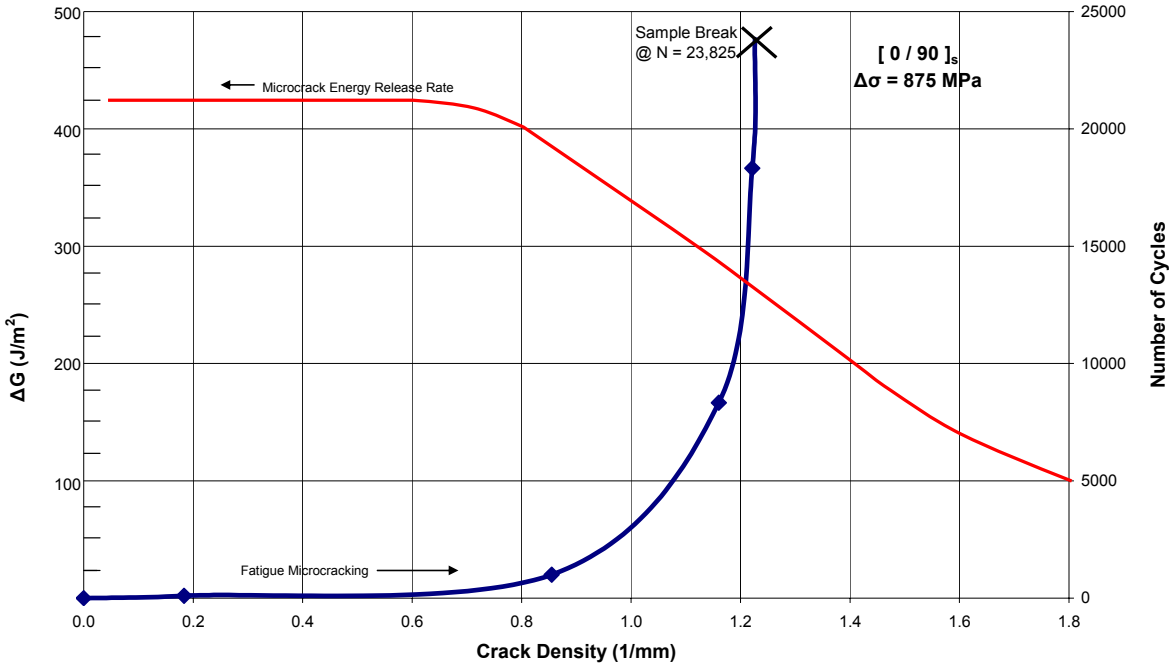

Figure 17: Microcracking Fatigue to Failure Data for Specimen 2-I-IV-3 showing the effects of crack saturation caused by decreasing energy release rate

One problem with conventional fatigue experiments is that both crack length, the dependent variable, and ΔK, the independent variable are changing. However, for microcracking fatigue experiments we can take advantage of the fact that ΔG is constant for a wide range of microcrack densities. Therefore, it is a relatively simple

matter to measure crack density as a function of cycle number for a series of constant $\Delta\sigma_0$ values.

It is expected that microcrack density will increase linearly with cycle number up to between 0.75 to 0.80 mm^{-1} microcrack density and thereafter begin to rapidly level off because ΔG is relatively constant up to that density. In reality, there is observed a rapid increase to some microcrack density after which microcrack density does indeed increase linearly with cycle number. It is believed that the initial microcracking is caused by the presence of inherent flaws in the laminate caused by initial manufacturing imperfections.

The preceding observations lead to the plot of microcrack density versus cycle number to be divided into three regions as discussed in section 1.1 and shown previously with Figure 3. These regions are the flaw dominated region, the constant growth region, and the slow growth region. In the flaw dominated region, the first microcracks form at flaws during the first, relatively low number of, cycles. This cracking is driven by laminate, or specimen, quality and is difficult to characterize. Because the energy release rate in equation (1) does not account for the presence of flaws, it cannot be used to predict behavior in the flaw dominated region. In the constant growth region, cracks have formed at all of the inherent flaws and new cracks are formed according to the Paris Law as described by equation (10). ΔG is constant in this region, so crack density increases linearly with cycle number at a slope dominated by the inherent toughness of the material system. The slow growth region is reached when the microcrack density increases enough to suppress ΔG. It is predicted

according to equation (10) that as ΔG decreases, so will the slope of the crack density curve. This is exactly what is observed [16].

The observed distribution of microcracks during testing is also worth noting. While microcracks did tend to form in evenly spaced intervals, they were not evenly distributed across the length of the specimen. Microcracking typically began near one end of the specimen. When the local crack density near that end reached some critical value, then cracks would be observed at the opposite end. Likewise, when cracking at the opposite end reached some critical local density then cracking would be observed in the center. Most specimens followed this pattern of crack formation.

3.4 Constant Growth Region

Both ΔG and the slope of the crack density versus cycle number curve are constant in the constant growth region. It is therefore advantageous to measure crack density growth rate as a function of applied ΔG in this region. Prior to the experiments, the microcrack density at which ΔG begins to decline was determined using equation (1). This crack density was determined to be 0.75 mm^{-1} and was set as the endpoint of the tests. Since little useful information was to be gained in the flaw dominated region it was not necessary to gather much data there. The objective of each test was to gather as much data in the constant growth region as possible so as to provide confidence for slope calculations. This objective was accomplished with differing levels of success from specimen to specimen due to the difficulty of knowing, *a priori*, the crack density growth rate. However, the specimens where many data points were obtained in the region between 0.25 to 0.75 mm^{-1} all exhibited definite linear behavior. This fact lends credence to the theory that the crack density growth rate is a function of ΔG as

described in equation (10). The remainder of this section contains figures showing the constant growth region microcrack density growth rates and test specific observations for the specimens tested in this study.

Preliminary studies were performed on specimens 2-I-IV-1, 2-I-IV-2, 2-I-IV-3, and 2-I-IV-4. Specimen 2-I-IV-2 was the first specimen tested where microcracking data was obtained. For this specimen, the peak applied load, $\Delta\sigma_0$, was 1096 MPa which corresponds to an applied microcrack energy release rate, ΔG_m, of 605 J/m^2. The specimen failed in the tab during the second cycle, before peak load. The one data point obtained corresponded to a crack density of 1.83 cracks per centimeter at one cycle. Note that this one point is not located in the 0.25 mm^{-1} to 0.75 mm^{-1} range of interest.

Specimen 2-I-IV-3 was the first specimen tested with any success. For this specimen, the peak applied load, $\Delta\sigma_0$, was 875 MPa which corresponds to an applied microcrack energy release rate, ΔG_m, of 427 J/m^2. Unfortunately only two data points, the endpoints, are available near the constant growth region. The first endpoint has a microcrack density of 0.183 mm^{-1} at 100 cycles. However, because the second endpoint is outside of the expected linear region with 0.855 mm^{-1} at 1000 cycles, the slope is underestimated. This specimen was inspected at 100, 1000, 8325, and 18325 cycles. This specimen failed at 23,825 cycles and reached a microcrack saturation density of 1.23 mm^{-1}.

Specimen 2-I-IV-4 is somewhat anomalous relative to the remainder of the test bed due to the fact that the apparent linear region is outside of the crack density envelope predicted by equation (1). For this specimen, the peak applied load, $\Delta\sigma_0$, was

845 MPa which corresponds to an applied microcrack energy release rate, ΔG_m, of 406 J/m^2. The results for this specimen are shown in Figure 18. This specimen was inspected every 100 cycles in the apparent linear region. This specimen is where the oblique illumination technique was developed for optically detecting microcracks. Therefore, the latter data points have a greater basis of accuracy than the earlier. Alternately, initial manufacturing imperfections may have been more numerous than with the other specimens yielding a curve "shifted up" from its nominal position. Regardless, the data from this specimen is suspect and the slope was not reported in the master plot, Figure 28, and was not included in the regression analysis.

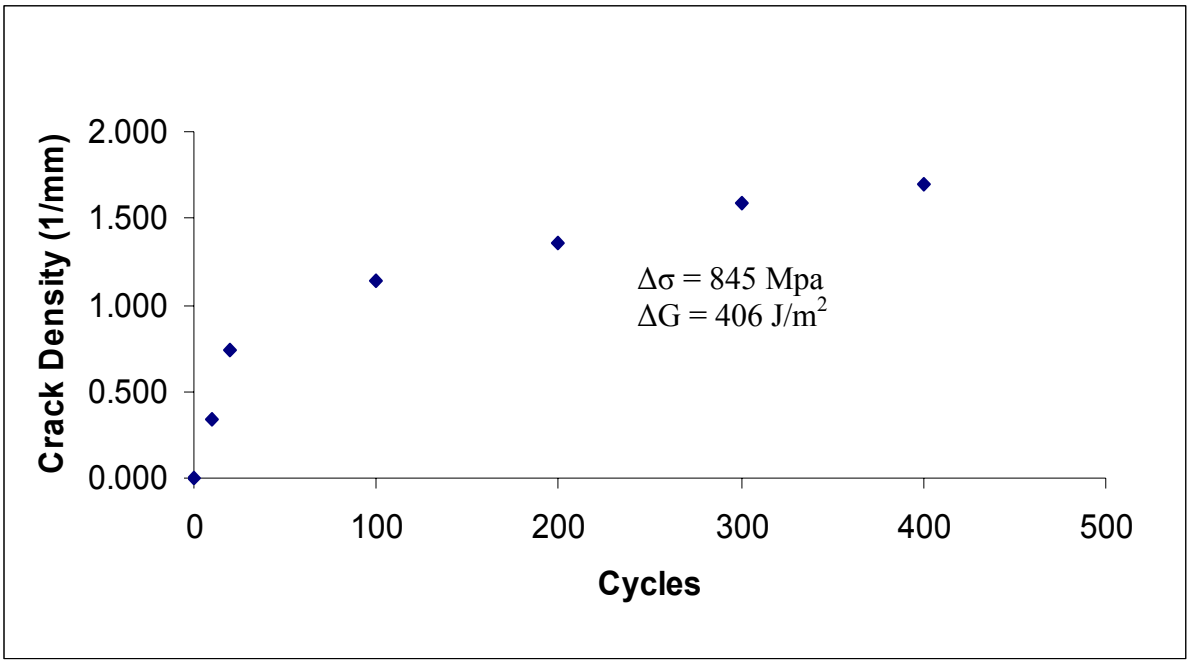

Figure 18: Specimen 2-I-IV-4 Fatigue Microcracking Data for peak cyclic load of 845 MPa corresponding to an applied energy release rate of 406 J/m^2

Specimen 2-I-IV-5 has only three data points in the linear region, the results for which are shown in Figure 19. For this specimen, the peak applied load, $\Delta\sigma_0$, was 810 MPa which corresponds to an applied microcrack energy release rate, ΔG_m, of 381 J/m^2. However, unlike the previous specimen, all data was gathered with the oblique

illumination technique and the apparent linear region lays within the expected envelope. Additionally, the intermediate data point at 1000 cycles lies almost exactly on the line between the two endpoints. This specimen is the first where the crack density growth rate is reported with good confidence. Also, observe the shallow slope of the curve in the flaw dominated region. This specimen was inspected at 100, 500, 1000, and 2000 cycles.

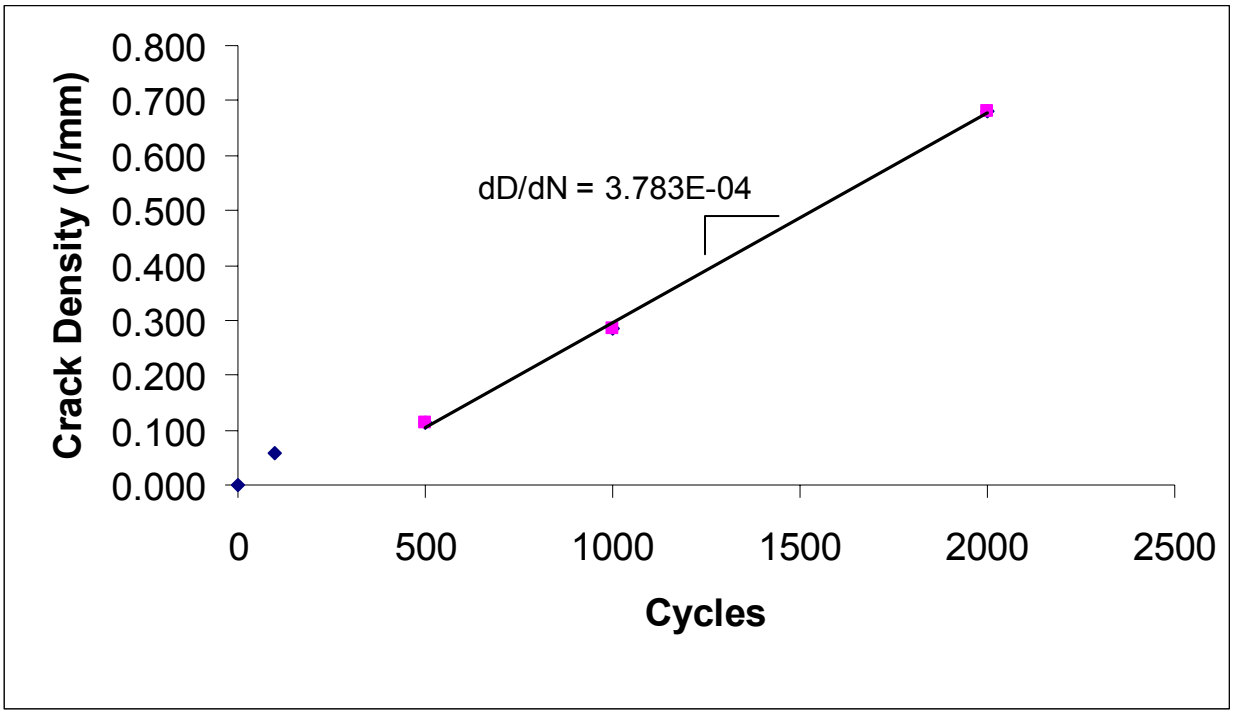

Figure 19: Specimen 2-I-IV-5 Constant Growth Region for peak cyclic load of 810 MPa corresponding to an applied energy release rate of 381 J/m^2

Specimen 2-I-IV-6, like the previous specimen, exhibits a relatively shallow slope in the flaw dominated region, the results for which are shown in Figure 20. For this specimen, the peak applied load, $\Delta\sigma_0$, was 630 MPa which corresponds to an applied microcrack energy release rate, ΔG_m, of 266 J/m^2. This shallow slope created an erroneous expectation that the cycle duration of the linear region would be larger than it was. This caused fewer data points to be taken in the linear region than was optimal.

This specimen was inspected at 2000, 5000, 10000, 185000, and 35166 cycles. This specimen failed at 35,166 cycles and reached a saturation microcrack density of 1.41 mm^{-1}.

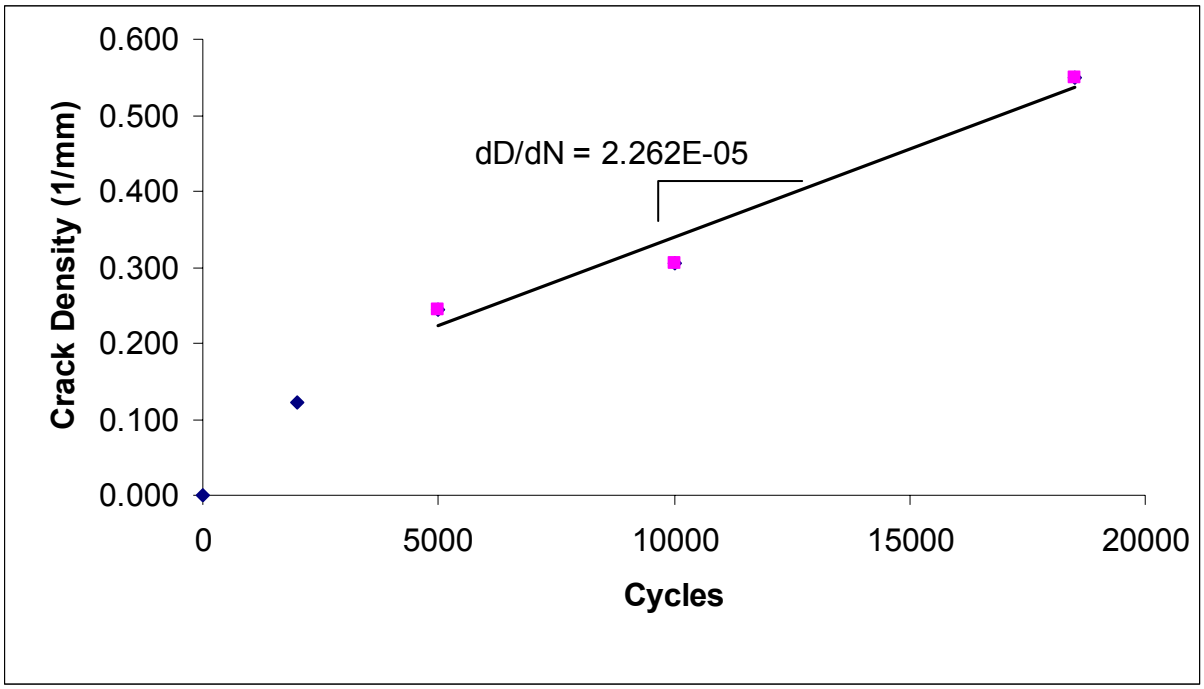

Figure 20: Specimen 2-I-IV-6 Constant Growth Region for peak cyclic load of 630 MPa corresponding to an applied energy release rate of 266 J/m^2

Specimen 2-I-IV-7 is a low stress, high cycle fatigue specimen, the results for which are shown in Figure 21. For this specimen, the peak applied load, $\Delta\sigma_0$, was 511 MPa which corresponds to an applied microcrack energy release rate, ΔG_m, of 202 J/m^2. The data collected for this specimen is theoretically in the flaw dominated region. As shown in Figure 21, at 300,000 cycles the microcracking density is below 0.2 mm^{-1}.

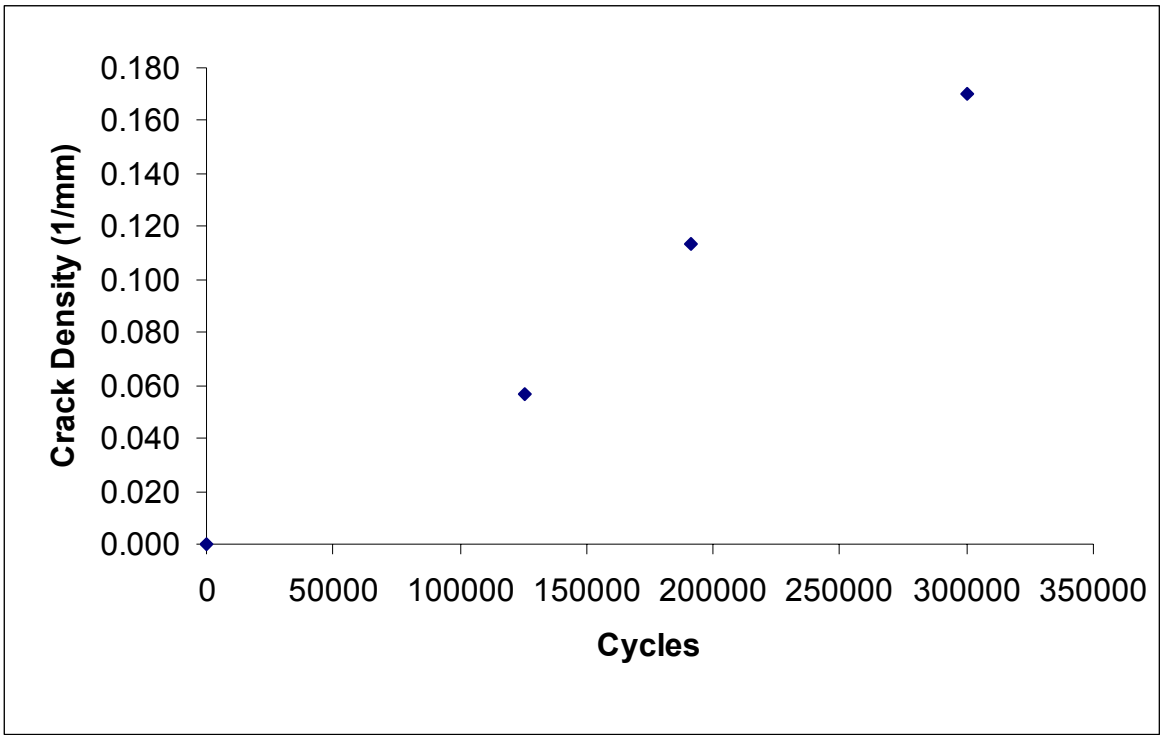

Figure 21: Specimen 2-I-IV-7 Fatigue Microcracking Data for peak cyclic load of 511 MPa corresponding to an applied energy release rate of 202 J/m^2

Specimen 2-I-IV-8 was the first specimen where many data points were gathered in the constant growth region, the results for which are shown in Figure 22. For this specimen, the peak applied load, $\Delta\sigma_0$, was 850 MPa which corresponds to an applied microcrack energy release rate, ΔG_m, of 409 J/m^2. This specimen was inspected every 25 cycles in the constant growth region. The eight data points gathered show that the crack density growth rate is constant between the flaw dominated region and the slow growth region. This constant slope lends confidence in equation (10) and the theory that a constant applied ΔG will result in a linear plot in the constant growth region. This specimen is the first where the crack density growth rate is reported with excellent confidence.

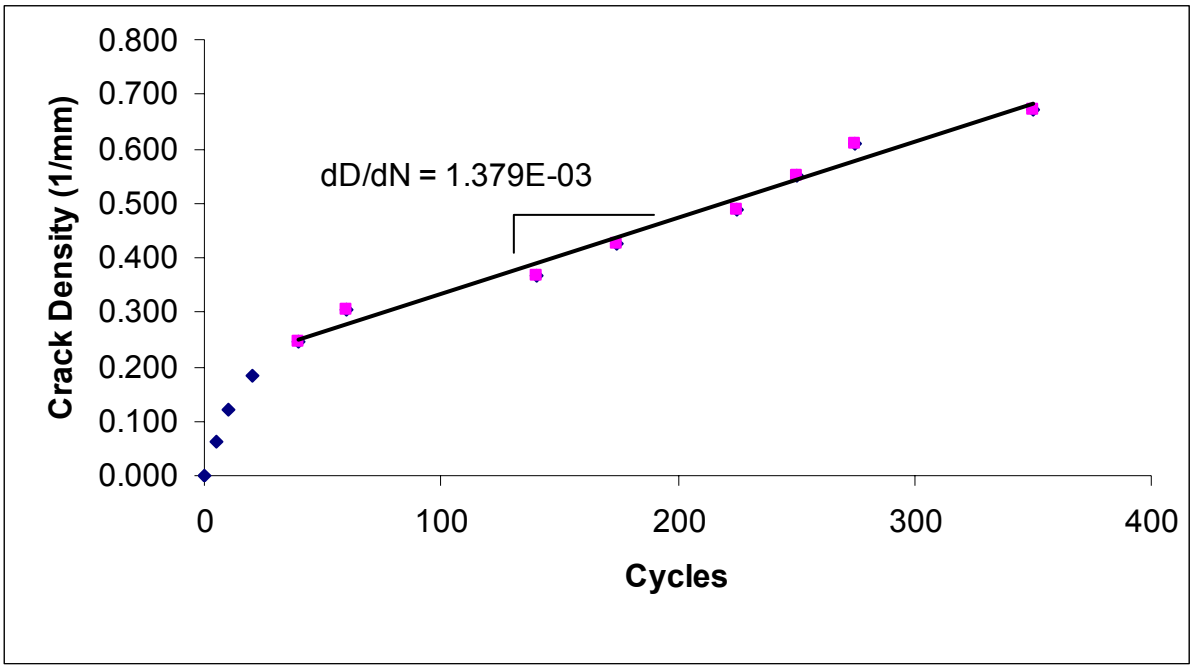

Figure 22: Specimen 2-I-IV-8 Constant Growth Region for peak cyclic load of 850 MPa corresponding to an applied energy release rate of 409 J/m^2

Specimen 2-I-IV-9 has a high number of data points in the linear region lending confidence to the reported slope, the results for which are shown in Figure 23. For this specimen, the peak applied load, $\Delta\sigma_0$, was 955 MPa which corresponds to an applied microcrack energy release rate, ΔG_m, of 488 J/m^2. Also, observe the shallow slope in the flaw dominated region. This specimen was inspected every 20 cycles in the constant growth region.

Specimen 2-I-IV-10, the results for which are shown in Figure 24, is a low cycle fatigue specimen with a very high slope in the flaw dominated region and sufficient data in the constant growth region to be confident in the reported slope. For this specimen, the peak applied load, $\Delta\sigma_0$, was 1030 MPa which corresponds to an applied microcrack energy release rate, ΔG_m, of 549 J/m^2. This specimen was inspected at 5, 15, 40, and 50 cycles.

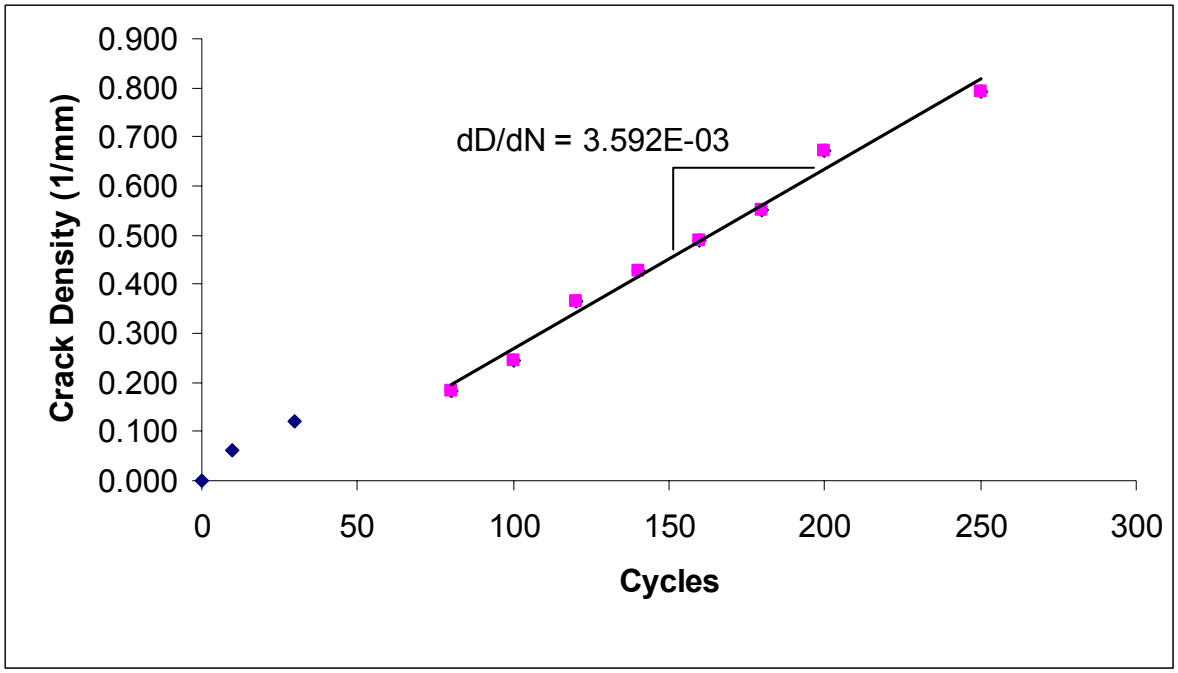

Figure 23: Specimen 2-I-IV-9 Constant Growth Region for peak cyclic load of 955 MPa corresponding to an applied energy release rate of 488 J/m^2

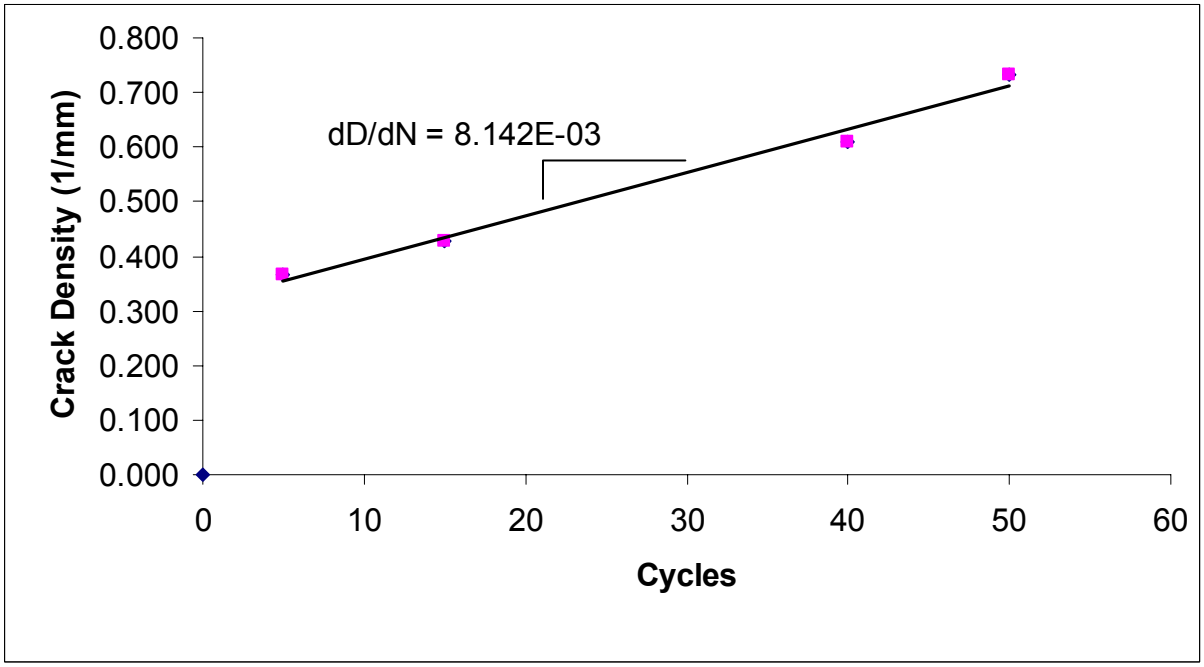

Figure 24: Specimen 2-I-IV-10 Constant Growth Region for peak cyclic load of 1030 MPa corresponding to an applied energy release rate of 549 J/m^2

Specimen 2-I-IV-11 is a high stress, low cycle fatigue specimen, the results for which are shown in Figure 25. The peak cyclic stress for this specimen, 1095 MPa, was chosen to correspond as closely as possible to the static microcrack fracture toughness, G_{mc} = 600 J/m$_2$. The actual applied microcrack energy release rate, ΔG_m, for this specimen was 605 J/m^2. This is the highest stress tested in this study and represents an upper bound on the applicability of the Paris Law. The very high slope of the flaw dominated region may not be due entirely to the presence of inherent flaws in the material. Eight microcracks were observed after the first cycle and it is likely some of them were due to the critical microcrack energy release rate being exceeded locally. This specimen was inspected every 5 cycles in the constant growth region.

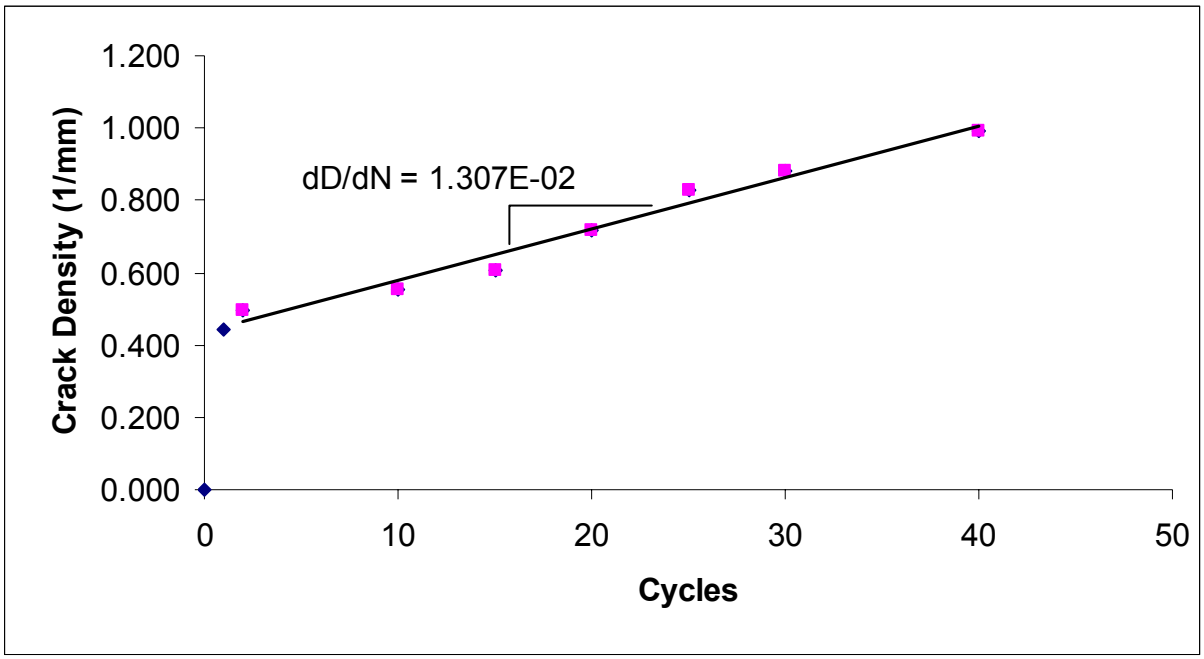

Figure 25: Specimen 2-I-IV-11 Constant Growth Region for peak cyclic load of 1095 MPa corresponding to an applied energy release rate of 605 J/m^2

Specimen 2-I-IV-12 is another specimen that exhibits unexpected behavior in the flaw dominated region, the results for which are shown in Figure 26. For this specimen,

the peak applied load, $\Delta\sigma_0$, was 740 MPa which corresponds to an applied microcrack energy release rate, ΔG_m, of 334 J/m^2. This specimen was inspected every 1000 cycles. Unfortunately, this specimen has only three data points in the linear region and they do not align as well as would be hoped. This lack of alignment can be shown to be due to the lack of one microcrack where it was expected. Or, alternately, the alignment is due to the fact that the crack density increased prior to optical microscopic inspection. See section 3.5 Sources of Error below for further discussion on this topic.

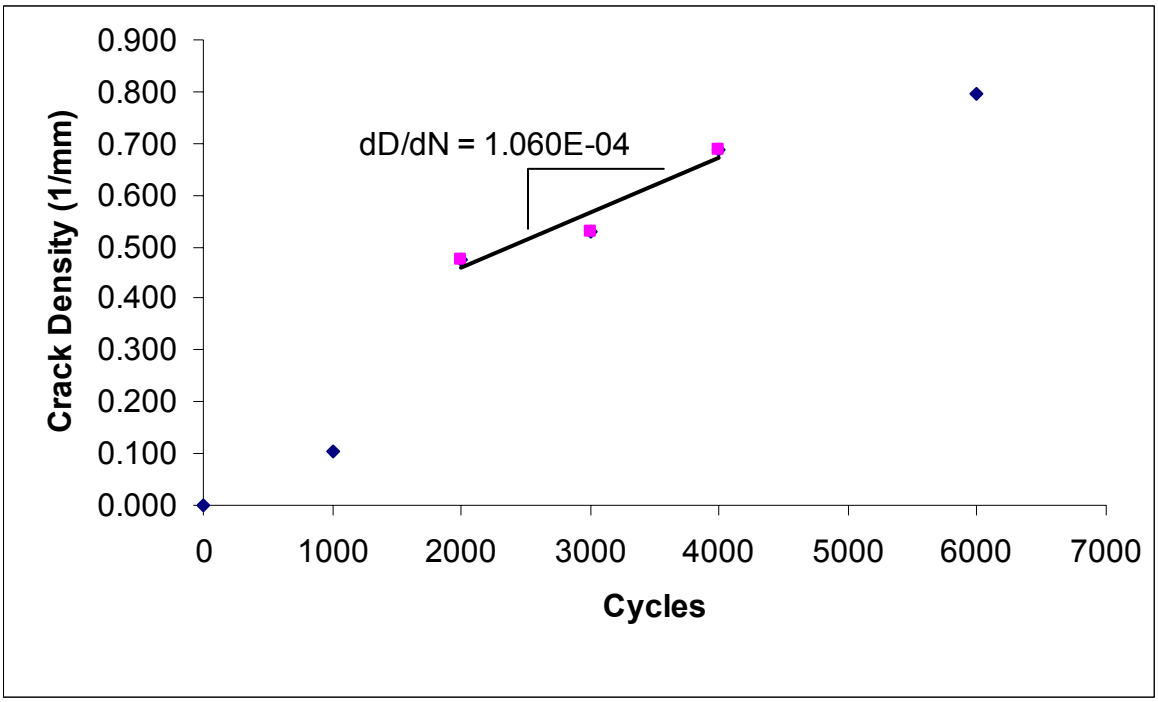

Figure 26: Specimen 2-I-IV-12 Constant Growth Region for peak cyclic load of 740 MPa corresponding to an applied energy release rate of 334 J/m^2

3.5 Sources of Error

The greatest sources of error lay within the difficulty of characterizing microcrack density as a function of cycle number. Microcracking, cycling, and inspection, all intimate aspects of the current study, are in fact discrete events. Meaning that they all happen at a specific moment in time and are not continuous across ranges of an

independent variable. For example, there is no such thing as 2.4 microcracks or cycles either. Another example is when inspecting a specimen at a given cycle number and observing a certain number of microcracks. The observed number of microcracks may have been manifest at much earlier cycles, while the next microcrack my happen in the next few cycles. In both cases the slope will be underestimated. For instance, specimen 2-I-IV-5 has three data points in the constant growth region. At 2000 cycles 12 microcracks are observed. If all 12 of these cracks were actually manifest at 1900 cycles, then the true slope would be 4.053×10^{-4} mm^{-1} as opposed to the reported slope of 3.783×10^{-4} mm^{-1}. On a log – log plot, this would represent an error of 0.88%. If the 13^{th} crack formed at 2020 cycles, then the true slope would be 4.106×10^{-4} mm^{-1} as opposed to the reported slope of 3.783×10^{-4} mm^{-1}. On a log – log plot, this would represent an error of 1.05%. The damage accumulation model inherent to the Paris Law approach assumes that crack density is differentiable over a range of cycles. While this is useful from an engineering standpoint, mathematically it is a *non sequitur*. For these reasons, all reported curve slopes and fitting parameters should be considered as approximations.

Difficulties associated with the detection of microcracks constitute additional sources of error. The method of microcrack detection used in this study was optical microscopy. Any cracks that existed internally to the specimen, but did not form at the single edge under inspection would not be observed at all. Likewise, a surface defect or very shallow surface crack could be mistaken as a through width microcrack. Also, due to physical space limitations, it was impossible to see the entire length of any specimen. Any cracks that formed outside of the visible area, called the optical length, were not

counted. Finally, as mentioned previously, prior to the development of the oblique illumination technique some cracks may have been too fine to observe under the small pre-load and direct lighting for specimens 2-I-IV-2, 2-I-IV-3, and 2-I-IV-4.

A final source of error is the reliability of the mechanical properties listed in table 2. These properties were gathered from diverse sources and some, such as transverse Poisson's ratio, are notoriously difficult to measure. Also, the coefficients of thermal expansion are not reported for IM7/977-2, but instead are generic values for graphite/epoxy laminates. For example, a 10% error in transverse CTE results in a 4% error in calculated G_{mc}.

3.6 Observations

The point at which the crack density versus cycle number plot becomes linear and enters the constant growth region was not consistent in this study, but was typically around 0.25 mm^{-1} microcrack density. According to equation (1), the end of the constant growth region is 0.75 mm^{-1} microcrack density. Therefore, the typical constant growth region is between 0.25 mm^{-1} and 0.75 mm^{-1} microcrack density.

Microcrack saturation before failure was observed in both static and fatigue loading experiments. In the previous work done on IM7/977-2, microcrack density was observed to saturate at around 1.3 mm^{-1} before failure [6, 13]. In this study, while only two specimens were cycled to failure, the microcrack saturation density varied, but also approached 1.3 mm^{-1} before failure. Table 5 contains microcrack saturation data for the specimens that were cycled to failure. Figure 27 shows a graph of the number of cycles to failure for these specimens. Note that the data point at 0 cycles represents the static ultimate capability for these cross-ply laminates.

Table 5: Microcrack Saturation to Failure

Specimen	Load (MPa)	ΔG (J/m2)	# of Cycles to Failure	Crack Saturation (mm^{-1})
2-I-IV-6	630	266	35,166	1.41
2-I-IV-3	875	427	23,825	1.23

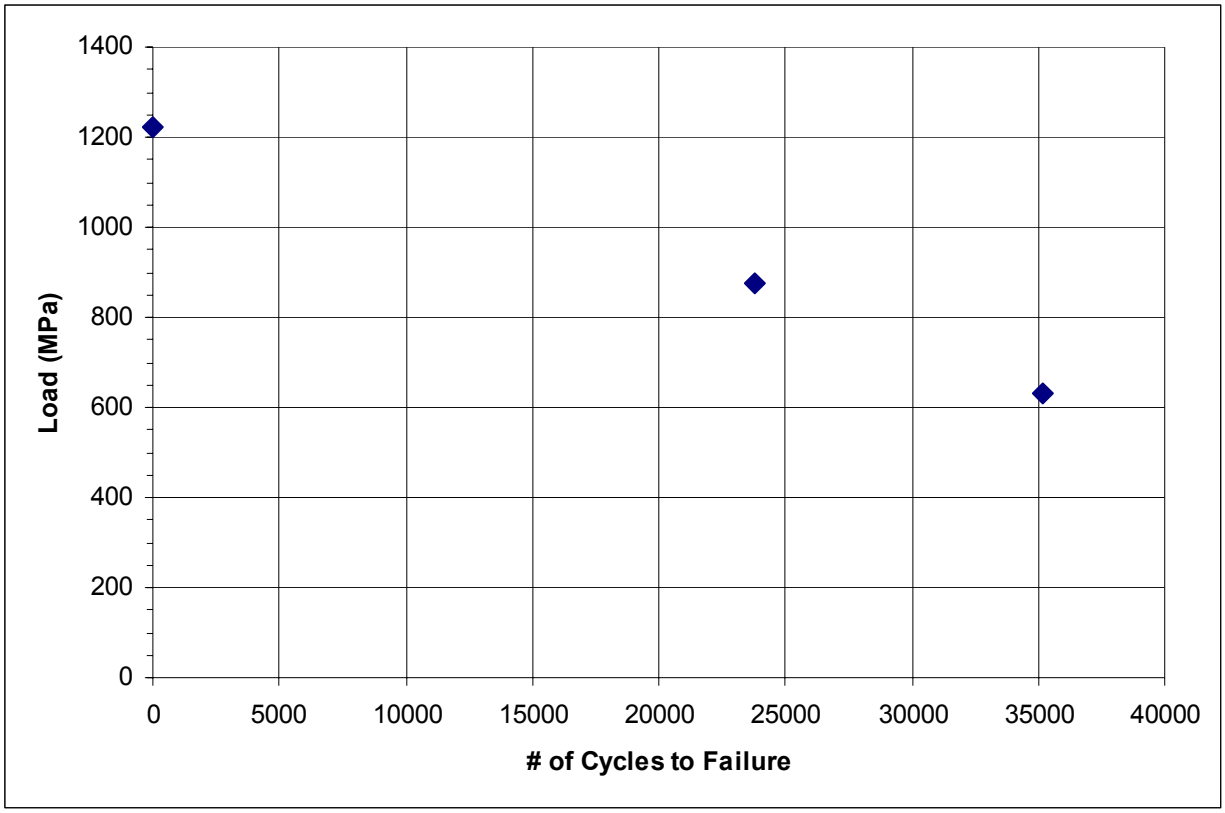

Figure 27: Number of Cycles to Failure for IM7/977-2 $[0/90]_s$ Laminates

Also of interest is the number of cycles to initiate the first microcrack in each of the samples tested. This would be of special interest in an application where absolutely no permeation would be acceptable. In that case, it would be possible to design a life cycle margin before the onset of the first microcrack. Therefore, there would be no microcracking and no permeation. However, such an approach may not be realistic as the laminate may need to be built up beyond the strength requirement and thereby

eliminate any weight savings. For some specimens, the number of cycles to the first microcrack was observed directly. For others, the number of cycles to the first microcrack was interpolated from observed data. The results are presented in table 6.

Table 6: Number of Cycles to First Microcrack

Specimen	Load (MPa)	ΔG (J/m^2)	# of Cycles to N_{mc} = 1
2-I-IV-7	511	202	125,500
2-I-IV-6	630	266	1000
2-I-IV-12	740	334	500
2-I-IV-5	810	381	100
2-I-IV-8	850	409	5
2-I-IV-9	955	488	10
2-I-IV-10	1,030	549	1
2-I-IV-11	1,095	605	1

It may also be of interest to note the number of cycles required to reach five cracks per centimeter, the nominal center of the constant growth region. While no data was taken at exactly 0.50 mm^{-1}, it is possible to calculate these numbers of cycles using actual data and a point-slope interpolation. The results of these calculations are presented in table 7.

Table 7: Calculated Number of Cycles to Five Cracks per Centimeter

Specimen	Load (MPa)	ΔG (J/m^2)	# of Cycles to D = 0.5 mm^{-1}
2-I-IV-6	630	266	16,306
2-I-IV-12	740	334	2,219
2-I-IV-5	810	381	1,522
2-I-IV-8	850	409	204
2-I-IV-9	955	488	168
2-I-IV-10	1,030	549	21
2-I-IV-11	1,095	605	2

3.7 Discussion of Paris Law Results

Equation (10) has shown to be valid for other graphite/epoxy materials as discussed previously in section 1.4.2 and if this equation is valid for IM7/977-2, then a plot of *dD/dN* as a function of *ΔG* should appear linear on a log – log plot. It can be observed from Figure 28 that the relationship is in fact linear over a wide range. After regression analysis (see Appendix A), this relationship can be quantitatively described as:

$$\frac{dD}{dN} = 6.40 \times 10^{-25} \left(\Delta G\right)^{8.07} \tag{11}$$

The fitting parameter A = 6.40 x 10^{-25}, represents the y intercept on a log – log plot. The fitting parameter B = 8.07 represents the slope of the line on a log – log plot. Specimen 2-I-IV-7 is shown on Figure 28 as a circled red data point. All of the data collected for this specimen is in the theoretical flaw dominated region below 0.2 mm^{-1}. Because the data is not obviously in the constant growth region, there is poor confidence that the reported slope is valid for equation (10). Though other specimens have shown a shallow slope in the flaw dominated region, namely 2-I-IV-5 and 2-I-IV-9, this region is expected to have a steeper slope than the constant growth region. The slope in the flaw dominated region for 2-I-IV-7 is well below the predicted slope in the constant growth region as shown in the master plot, Figure 28. This is an indication that 202 J/m^2 may be near the threshold microcrack fracture toughness and that the curve is in Region I. This datum was reported as an outlier in the Paris Law plot for information purposes only and was not used in the regression analysis.

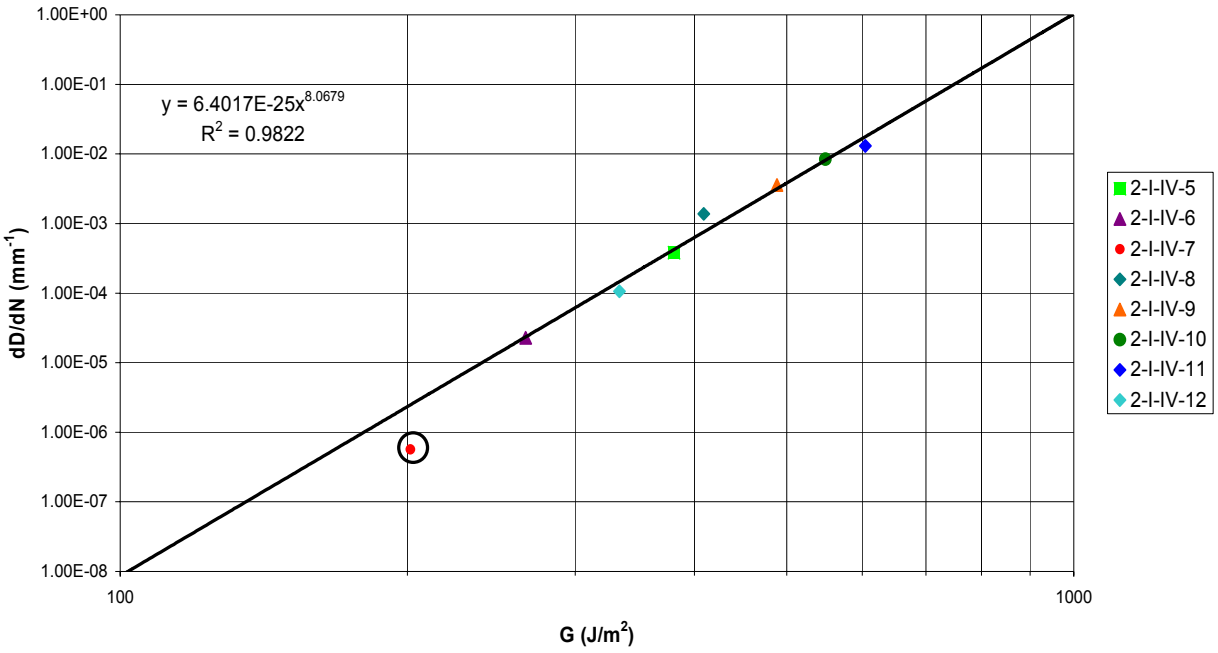

Figure 28: Modified Paris Law Results for Material IM7/977-2 in Fatigue

The slope of the Paris Law curve for IM7/977-2 is much steeper than those for other laminates tested previously by Liu and Nairn [16]. The previously tested materials had slopes of 5.47 for IM6/Avimid K (graphite/polyimide) and 2.34 for T300/934 (graphite/epoxy), while the slope for IM7/977-2 is 8.07. This indicates that the microcrack density growth rate for IM7/977-2 is much more sensitive to changes in ΔG, and by extension $\Delta\sigma_0$, than the other materials tested. Comparing IM7/977-2 to the other graphite/epoxy tested earlier, T300/934, it is clear that IM7/977-2 has a much wider range of the Paris Law Region II. Region II is the area of applicability for the power law associated with Paris [28]. The graphite/epoxy tested by Liu clearly exhibits Region I, Region II, and Region III behavior with a shallow slope between 300 J/m^2 and 600 J/m^2, and with very steep slopes in both Regions I and III. The data for both materials previously tested by Liu indicates that Region II ends at the static microcrack fracture toughness, G_{mc}, beyond which exists Region III. The data presented here for

IM7/977-2 is entirely in the “linear” region, or Region II, of the Paris Law and extends from 266 J/m^2 to 605 J/m^2. The upper limit of the observed linear region, 605 J/m^2, is very close to the static microcrack fracture toughness for IM7/977-2, 600 J/m^2, and it is expected that testing above this value would show non-linear growth. Likewise, the graphite/epoxy material previously tested by Liu demonstrated a threshold at 300 J/m^2 below which very steep Region I growth took place. While it may be that, upon completion of testing, specimen 2-I-IV-7 will be in Region I and fall below the Paris Law curve, it is still too early to be sure. If this is the case, the threshold between Region I and Region II will be between 266 J/m^2 and 202 J/m^2.

It should be noted, that while it is possible to say that IM7/977-2 is more sensitive to *changes* in ΔG due to the steeper slope in region II, it is not possible to really compare applied G_m or G_{mc} from one material to another. The reason being that G_m as a function of applied load, temperature, etc., is highly dependent on material properties. For example, a load of 188.4 MPa applied to a $[0_2/90_4]_s$ laminate of T300/934 results in a G_m of 350 J/m^2. By comparison, to achieve a G_m of 350 J/m2 in a $[0_2/90_4]_s$ laminate of IM7/977-2 requires 587 MPa. This is because T300/934 is a much weaker material than IM7/977-2.

4.0 Conclusions and Recommendations

The log – log plot is linear indicating that equation (10) holds true over a wide range of ΔG. The linear fitting parameter, R^2, for this plot is 0.98 indicating that the fitting parameters are excellent predictors of microcrack density across the tested range of ΔG. The power law coefficient in this range is $A = 6.40 \times 10^{-25}$ and the power law exponent is B = 8.07 in this range.

The upper limit of applicability for equation (11) is 605 J/m^2, corresponding to $\Delta\sigma_0$ = 1095 MPa, which is within the margin of error to the static microcracking fracture toughness for this material system. Releasing energy above 600 J/m^2 requires strains near the strain to failure. Loading beyond the static microcrack fracture toughness creates additional problems and risks material failure. Also, the useful range for this equation is likely to be well below G_{mc} due to the application of a factor of safety to any realistic flight hardware. The lower limit of applicability for this equation is 266 J/m^2, corresponding to $\Delta\sigma_0$ = 630 MPa, Note that, for this material and a $[0/90]_s$ laminate, the number of cycles to failure for an initial applied ΔG = 266 J/m^2, corresponding to $\Delta\sigma_0$ = 630 MPa, is 35,166. A typical minimum for life cycle margin from failure is four mission lives for a damage tolerant material [29]. Therefore, equation (11) is applicable for a hypothetical cross-ply IM7/977-2 laminate designed to survive 8,800 limit load cycles. Also, equation (11) may be applicable at even lower stress and applied ΔG levels. Therefore, equation (11) envelops the useful range of realistic applied stresses for composite structures made from IM7/977-2 unidirectional tape and in theory it can be used to predict microcrack density growth for a variety of laminates loaded in fatigue.

Additional testing is required to verify the discovered power law fitting parameters are valid for a variety of laminates besides $[0/90]_s$ despite the excellent agreement between the modified Paris Law theory and experimental results from this study. It is recommended that similar testing programs be conducted for alternative cross ply lay-ups such as $[0/90_2]_s$ and $[0/90_4]_s$ as well as laminates with 90° plies on the outside to verify that equation (11) still holds. Additional experimental perturbations of interest include testing laminates at different frequencies, and also to extend the ΔG range to find the upper and lower threshold limits to the applicability of the Paris Law Region II.

More importantly, though, is the need to expand the generality of the energy based fracture mechanics approach to allow for analysis of more realistic laminates. Cross-ply $[0_n/90_m]_s$ laminates are rarely used for structures due to their poor off-axis properties. The ability to analyze balanced, symmetric, and quasi-isotropic laminates under bi-axial stress for microcracking fracture toughness might expand the acceptance and use of this approach throughout government and industry. Once a theoretical analytical technique for calculating microcracking energy release rate in general laminates is derived, it should be possible to apply the Paris Law damage accumulation approach to realistic lay-ups of simple structures through a finite element method. In turn, the analytical model could be verified through destructive testing of a test article. Finally, an analytical tool could be developed that models complex, realistic structures and launch vehicle thermal and mechanical load profiles to predict microcrack density and permeability at various points in the vehicle life cycle.

References

[1] Callister, W. D.; “Materials Science and Engineering An Introduction,” 5th ed., John Wiley & Sons, New York, 2000.

[2] MIL-HDBK-17F; “Composite Materials Handbook,” 2002.

[3] Beaumont, P. W. R.; “Pushing the Performance Limit of Composite Structures Part 1: Modeling,” *Reinforced Plastics*, p. 58-63, September 2006.

[4] Mallick, K.; et. al.; “An Integrated Systemic Approach to Linerless Composite Tank Development,” *Collection of Technical Papers – AIAA/ASME/ASCE/AHS/ASC Structures, Structural Dynamics and Materials Conference*, v 5, p. 3553-3569, 2005.

[5] Mallick, K.; et. al.; “Ultralight Linerless Composite Tanks for In-Space Applications,” *Collection of Technical Papers – AIAA Space 2004 Conference and Exposition*, v 1, p. 1-13, 2004.

[6] Verges, M. A.; et. al.; “Investigation of Microcrack Growth in $[0/90]_s$ Composite Laminates,” *ASME Pressure Vessels Piping Div. Publ.,* p.171-175, 2005.

[7] Nairn, John A.; “Matrix Microcracking in Composites,” *Polymer Matrix Composites*, Elsevier Science, R. Talreja and JA, Manson eds., Chapter 13, 2001.

[8] Smith, P. A.; Boniface, L.; Glass, N. F. C.; “A Comparison of Transverse Cracking Phenomena in (0/90)s and (90/0)s CFRP Laminates,” *Applied Composite Materials*, v. 5, p. 11-23, 1998.

[9] Liu, S.; Nairn, J. A.; “The Formation and Propagation of Matrix Microcracking in Cross-Ply Laminates During Static Loading,” *Journal of Reinforced Plastics and Composites*, v. 11, p. 158-178, 1992.

[10] Nairn, J. A.; Hu, S.; Bark, J. S.; “A Critical Evaluation of Theories for Predicting Microcracking in Composite Laminates,” *Journal of Material Science*, v. 28, p. 5099-5111, 1993.

[11] Kim, H. W.; “Physical Aging Effects on the Microcracking Toughness in Advanced Composites,” *Ph.D. Thesis, University of Utah*, 1996.

[12] Yalvac, S.; Yats, L. D.; Wetters, D. G.; “Transverse Ply Cracking in Toughened and Untoughened Graphite/Epoxy and Graphite/Polycyanate Crossply Laminates,” *Journal of Composite Materials*, v. 25, p. 1653-1667, 1991.

[13] Hottengada, B.; “Investigation of Microcracking and Damage Propagation in Cross-Ply Composite Laminates,” *Thesis Submitted to the University of New Orleans in partial fulfillment of the requirements for the degree of Master of Science*, May 2006.

[14] Kim, H. W.; Grayson, M. A.; Nairn, J. A.; “The Effect of Hygrothermal Aging on the Microcracking Properties of Some Carbon Fiber/Polyimide Laminates,” *Advanced Composite Letters 4*, p. 185-188, 1995.

[15] Nairn, J. A.; Han, M. H.; “Hygrothermal Aging of Polyimide Matrix Composite Laminates,” *Proceedings of the ICCM 12 Paris*, 1999.

[16] Liu, S.; Nairn, J. A.; “Fracture Mechanics Analysis of Composite Microcracking: Experimental Results in Fatigue,” *Proceedings of the 5th Technical Conference on Composite Materials, American Society of Composites*, p. 287-295, 1990.

[17] Kessler, S.; et. al.; “Cryocycling and Mechanical Testing of CFRP fro the X-33 Liquid H2 Fuel Tank Structure” *ASC*, v. 93, 2001.

[18] Boniface, L.; Ogin, S. L.; “Application of the Paris Equation to the Fatigue Growth of Transverse Ply Cracks,” *Journal of Composite Materials*, v. 23, p. 735-754, 1989.

[19] Lee, J. K.; “Alternative Carbon Fiber Reinforced Polymer (CFRP) Composites for Cryogenic Applications,” *Thesis Submitted to Mississippi State University in partial fulfillment of the requirements for the degree of Master of Science*, May 2004.

[20] Beaumont, P. W. R.; “Pushing the Performance Limit of Composite Structures Part 2: Cracking Models,” *Reinforced Plastics*, p. 30-36, December 2006.

[21] Ganpatye, A. S.; Kinra, V.K.; “Ultrasonic Ply-by-Ply Detection of Matrix Cracks in Laminated Composites,” *Thesis Submitted to Texas A&M University in partial fulfillment of the requirements for the degree of Master of Science*, December 2005.

[22] Hu, S.; Bark, J. S.; Nairn, J. A.; “On the Phenomenon of Curved Microcracks in $[(S)/90_n]_s$ Laminates: Their Shapes, Initiation Angles and Locations,” *Composites Science and Technology*, v. 47, p. 321-329, 1993.

[23] Arzberger, S.; et. al.; “Strain to Initiate Microcracking in Materials for Linerless Composite Cryogenic Tanks,” *Space Cryogenics Workshop, Colorado Springs, CO*, August 2005.

[24] Mallick, K.; Arzberger, S.; “Hybrid Polymer Nanocomposites for Linerless, Composite Tanks,” *Presented at the Cryotanks Workshop National Space and Missile Materials Symposium*, 2005.

[25] Nairn, J. A.; Hu, S.; “The Formation and Effects of Outer-Ply Microcracks in the Cross-Ply Laminates: A Variation Approach,” *Engineering Fracture Mechanics*, v. 41, p. 203-221, 1992.

[26] VanPelt, J.; “Effect of Strain on the Gas Permeability of Composite Laminates,” *Thesis Submitted to the University of Florida in partial fulfillment of the requirements for the degree of Master of Science*, May 2004.

[27] Nairn, J. A.; “Fracture Mechanics of Composites with Residual Stresses, Imperfect Interfaces, and Traction-Loaded Cracks,” *Composites Science and Technology*, v. 61, p. 2195-2167, 2001.

[28] Paris, P.; Erdogan, F.; “A Critical Analysis of Crack Propagation Laws,” *Journal of Basic Engineering*, Trans. ASME, Series D, 85, 528 (1963).

[29] Anderson, T. L.; “Fracture Mechanics: Fundamentals and Applications,” 2nd ed., CRC, 1994.

[30] Su, X.; Abdi, F.; Lavoie, J.; “Prediction of Micro-crack Densities in Cryogenic IM7/977-2 Propellant Tanks,” *Proceedings of the 45th AIAA/ASME/ASCE/AHS/ASC Structures, Structural Dynamics and Materials Conference*, 2004.

[31] Noh, J.; Whitcomb, J.; et. al.; “Prediction of Leakage Rate Through Damage Network in Cryogenic Composite Laminates,” *Proceedings of the 45th AIAA/ASME/ASCE/AHS/ASC Structures, Structural Dynamics and Materials Conference*, 2004.

[32] Cytec Engineering Materials CYCOM 977-2 Material Data Sheet, 1995.

[33] ANSI/AIAA-S-081A-2006, “Composite Overwrapped Pressure Vessels (COPVs).”

[34] ANSI/AIAA-S-089-DRAFT, “Composite Pressurized Structure (CPS),” 2006.

Appendix A: Regression Analysis

The purpose of regression analysis is to find the values of the fitting parameters that minimize the variance between observed and predicted data. In this case, the function is a power law:

$$y = Ax^B$$

where y is the dependent variable, x is the independent variable, while A and B are the fitting parameters to be optimized. To perform a regression analysis of this equation, it is necessary to linearize this function. To do this, the natural log is taken of both sides of the equation such that:

$$\ln(y) = \ln(A) + B\ln(x)$$

Let there be a series of N observed data points corresponding to pairs (x_i,y_i). The variance between each observed data point and it's expected value is the square of the difference between them such that:

$$v_i = \{\ln(y_i) - [\ln(A) + B\ln(x_i)]\}^2$$

The total variance is the sum total of each individual variance such that:

$$v = \sum_{i=1}^{N} \{\ln(y_i) - \ln(A) - B\ln(x_i)\}^2$$

To minimize the total variance cause by parameter A, it will be sufficient to set the partial derivative of the variance with respect to A equal to zero. Likewise for parameter B. These two derivatives, being set to zero, will constitute a two equation and two unknown system. The derivatives being:

$$\frac{\partial v}{\partial A} = \sum_{i=1}^{N} [\ln(y_i) - \ln(A) - B\ln(x_i)] = 0$$

and

$$\frac{\partial v}{\partial B} = \sum_{i=1}^{N} \left\{ \left[\ln(y_i) - \ln(A) - B\ln(x_i) \right] \ln(x_i) \right\} = 0$$

For both equations, it is possible to isolate the ln(A) term. This leaves just one equation and one unknown such that:

$$\frac{1}{N}\sum_{i=1}^{N}\left[\ln(y_i) - B\ln(x_i)\right] = \frac{\sum_{i=1}^{N}\left\{\left[\ln(x_i)\right]\bullet\left[\ln(y_i)\right] - B\left[\ln(x_i)\right]^2\right\}}{\sum_{i=1}^{N}\left[\ln(x_i)\right]}$$

For any unique set of N pairs of (x_i,y_i) there is one, and only one value for B that satisfies this equation. This value for B can be found through a numerical iterative process. The value of A is dependent on the value of B.

The R^2 value is used to measure the fitness of a regression curve to the observed data and is always some fraction of 1. R^2 is defined as:

$$R^2 = 1 - \frac{SS_E}{SS_T}$$

where SS_E is the sum of squared errors and SS_T is the total sum of squares. Each is defined for the purposes of this study as follows:

$$SS_E = \sum_{i=1}^{N} \left\{ \ln(y_i) - \left[\ln(A) + B\ln(x_i) \right] \right\}^2$$

And

$$SS_T = \sum_{i=1}^{N} \left[\ln(y_i) - \overline{\ln(y_i)} \right]^2$$

Given a data set and the two derived fitting parameters, it is possible to calculate the R^2 value. Any value over 0.9 is generally considered to represent an excellent fit.

Vita

Michael Holt was born in Long Beach, CA and moved to the Greater New Orleans area in 1997, where he has stayed since. He received his Bachelor of Science in Mechanical Engineering with a Minor in Applied Mathematics from the University of New Orleans (UNO) in December 2004. He is a Materials Engineer for Lockheed Martin at NASA's Michoud Assembly Facility working in the field of composites on the Orion Crew Exploration Vehicle project and is performing graduate studies concurrently. He plans to pursue doctoral studies at UNO.